



A 10-Year Climatology of Tropical Radiative Heating and Its Vertical Structure from TRMM Observations

TRISTAN S. L'ECUYER AND GREG MCGARRAGH

Colorado State University, Fort Collins, Colorado

(Manuscript received 6 January 2009, in final form 11 August 2009)

ABSTRACT

This paper outlines recent advances in estimating atmospheric radiative heating rate profiles from the sensors aboard the Tropical Rainfall Measuring Mission (TRMM). The approach employs a deterministic framework in which four distinct retrievals of clouds, precipitation, and other atmospheric and surface properties are combined to form input to a broadband radiative transfer model that simulates profiles of upwelling and downwelling longwave and shortwave radiative fluxes in the atmosphere. Monthly, 5° top of the atmosphere outgoing longwave and shortwave flux estimates agree with corresponding observations from the Clouds and the Earth's Radiant Energy System (CERES) to within 7 W m^{-2} and 3%, respectively, suggesting that the resulting products can be thought of as extending the eight-month CERES dataset to cover the full lifetime of TRMM.

The analysis of a decade of TRMM data provides a baseline climatology of the vertical structure of atmospheric radiative heating in today's climate and an estimate of the magnitude of its response to environmental forcings on weekly to interannual time scales. In addition to illustrating the scope and properties of the dataset, the results highlight the strong influence of clouds, water vapor, and large-scale dynamics on regional radiation budgets and the vertical structure of radiative heating in the tropical and subtropical atmospheres. The combination of the radiative heating rate product described here, with profiles of latent heating that are now also being generated from TRMM sensors, provides a unique opportunity to develop large-scale estimates of vertically resolved atmospheric diabatic heating using satellite observations.

1. Introduction

Diabatic heating Q_1 plays a central role in driving atmospheric (ATM) variability on a wide range of time and space scales. The vertical structure of Q_1 has been shown to influence the atmosphere on scales ranging from the life cycle of individual mesoscale convective systems (e.g., Houze 1982, 1989; Mapes and Houze 1995) and the evolution of extratropical cyclones (Weaver 1999) to the propagation speed of tropical intraseasonal oscillations (e.g., Lau and Peng 1987; Lee et al. 2001) and the strength of the Hadley and Walker circulations (e.g., Slingo and Slingo 1988; 1991; Hartmann et al. 1984; Sherwood et al. 1994; Schumacher et al. 2004). The common conclusion to be drawn from these studies is the importance of feedback between clouds, precipitation, and their impact on atmospheric diabatic heating.

Understanding these feedback processes is critical for making progress in climate research (Stephens 2005; Bony et al. 2006).

Although regional estimates of Q_1 have been made from high time and space resolution observations of temperature and humidity profiles from enhanced sounding networks (e.g., Johnson and Ciesielski 2002; Zhang et al. 2001), global diabatic heating estimates on larger scales have, until now, primarily relied on model reanalyses. Given recent emphasis on evaluating model performance using observations, a strictly observation-based estimate of large-scale diabatic heating is highly desirable. As a result, the generation of satellite-based latent heating profile products that are consistent with instantaneous rainfall retrievals has been a goal of the Tropical Rainfall Measuring Mission (TRMM) since its launch (e.g., Tao et al. 1990, 1993; Smith et al. 1994; Shige et al. 2004, 2007; Grecu and Olson 2006). However, although the release of latent heat may dominate Q_1 locally in precipitating regions, estimating total atmospheric diabatic heating on larger scales and over

Corresponding author address: Tristan S. L'Ecuyer, Colorado State University, Fort Collins, CO 80523.
E-mail: tristan@atmos.colostate.edu

longer time periods requires coincident estimates of radiative cooling Q_R that account for surface (SFC) emissivity and albedo, vertical profiles of temperature and humidity, and the effects of nonprecipitating clouds. Moreover, several studies have demonstrated that, despite its smaller dynamic range, variations in Q_R may play a dominant role in modulating large-scale dynamics (e.g., Slingo and Slingo 1988, 1991; Sherwood et al. 1994; Tian and Ramanathan 2002, 2003).

A number of atmospheric radiative-heating products have been developed to date, ranging from high-quality regional Q_R products from Atmospheric Radiation Measurement (ARM) sites (McFarlane et al. 2007) to the satellite-based global, three-hourly, 280-km spatial resolution International Satellite Cloud Climatology Project (ISCCP)-FD product (Rossow and Lacis 1990; Zhang et al. 1995; Rossow and Zhang 1995; Bishop et al. 1997; Chen et al. 2000). Between these extremes, the Clouds and the Earth's Radiant Energy System (CERES) clouds and radiative swath (CRS) product (Wielicki et al. 1996) offers estimates of Q_R that are constrained to match top of the atmosphere (TOA) flux measurements but with reduced temporal sampling, whereas Cloudsat's level-2B radiative fluxes and heating rates algorithm (2B-FLXHR; L'Ecuyer et al. 2008) offers improved cloud boundary information and spatial resolution but at greatly reduced spatial and temporal sampling. All of these algorithms are built on the same basic framework that uses retrieved cloud properties as input to broadband radiative transfer calculations to simulate radiative flux profiles through the atmosphere; however, each makes trade-offs between spatial resolution, temporal sampling, spatial coverage, and the quality of its input datasets.

The Hydrologic Cycle and Earth's Radiation Budget (HERB) algorithm, described in detail in L'Ecuyer and Stephens (2003, hereafter LS03, 2007), strikes its own compromise between spatial resolution, vertical structure information, and spatial coverage, supplying Q_R products at 0.25° resolution over the region sampled by TRMM (38°N–38°S). The algorithm combines cloud, precipitation, and atmospheric and surface property information from the Visible And Infrared Scanner (VIRS) and TRMM Microwave Imager (TMI) instruments to establish vertical profiles of upwelling and downwelling longwave (LW) and shortwave (SW) radiative fluxes in the atmosphere. The resulting flux profiles are subsequently used to derive principal components of the radiation budget, profiles of radiative heating, and their breakdown into clear-sky and cloudy components. Although qualitatively similar to other satellite-based approaches, HERB offers the benefit of being directly tied to TRMM measurements, resulting in automatic co-registration with TRMM-based latent heating products.

In addition, its component algorithms provide an explicit representation of precipitation and independent low-cloud retrievals from microwave observations, providing a better representation of overlapping cloud systems than visible-infrared approaches.

The primary objectives of this paper are to provide an update of the HERB algorithm introduced in LS03, illustrate the character and duration of the resulting TRMM-based Q_R product and characterize its uncertainties, and document the 10-yr climatology of Q_R in the tropical and subtropical atmospheres and its variability on seasonal to interannual scales. Recent improvements to the HERB algorithm are described in section 2, including its extension to cover both land and ocean surfaces, the introduction of a time-resolved aerosol transport model, and superior cloud detection and retrieval algorithms. HERB products are evaluated in section 3 in the context of TOA flux measurements from the CERES and ground-based flux observations from a network of surface sites throughout the TRMM region. The 10-yr average climatologies of radiative fluxes and atmospheric properties from the HERB dataset are summarized in section 4, with the goal of establishing baseline TOA, SFC, and ATM radiation budgets and their spatial distribution across the TRMM domain. Particular emphasis is given to relating spatial gradients in energy balance to observed regional variability in the radiative impact of clouds. The effects of clouds on atmospheric radiative heating are further explored by adding a vertical dimension to the results in section 5. The 10-yr mean spatial distribution of atmospheric radiative heating and its temporal variability over four broad vertical levels are presented. Full vertical profiles of heating extracted over three oceanic and two continental regions are then explored in greater detail to illustrate the dramatically different character of Q_R under distinct cloud regimes.

2. HERB 2008

Core steps in the execution of the HERB algorithm remain similar to those described in LS03. Liquid- and ice-cloud properties are obtained from VIRS and TMI radiances using the algorithms described in Greenwald et al. (1993) and Cooper et al. (2003), respectively. Because the passive microwave radiances do not constrain particle size, a uniform effective radius of 11 μm is assumed for all liquid clouds consistent with the climatology of Miles et al. (2000). Unlike LS03, however, where all liquid clouds were assumed to reside between 0.5 and 1.5 km, the 2008 version of the algorithm (HERB 2008) assumes a cloud base of 0.5 km but uses the observed infrared (IR) brightness temperature from VIRS

to prescribe cloud top. Hydrometeor profiles in precipitating pixels continue to be prescribed based on the TMI-based TRMM 2A12 rainfall product (Kummerow et al. 2000), providing the most realistic representation of rainfall possible while maintaining the coverage of the wide TMI swath. Unlike LS03, however, IR brightness temperatures are now used to constrain cloud-top-mitigating potential uncertainties resulting from the lack of sensitivity of passive microwave observations to cloud ice.

These TRMM-based condensed water products are coupled with temperature, humidity, and ozone profiles from the National Centers for Environmental Prediction (NCEP) reanalysis (Kalnay et al. 1996) that have been further constrained by TMI-based sea surface temperature and column-integrated water vapor estimates from remote sensing systems (Wentz 1997; Wentz et al. 2000). The concentrations of less variable gases, such as carbon dioxide, are assumed to follow the McClatchey tropical atmosphere (McClatchey et al. 1972). These atmospheric properties are used as input to a broadband radiative transfer model known as BUGSrad (Ritter and Geleyn 1992; Stephens et al. 2001), which shares a heritage with those implemented in the Colorado State University (CSU) general circulation model (GCM) as well as the National Center for Atmospheric Research (NCAR) Community Climate Model (CCM). Within the HERB framework, BUGSrad accounts for scattering and absorption by cloud and precipitating liquid and ice particles and treats gaseous absorption by using the correlated k -distribution formulation of Fu and Liou (1992). A vertical resolution of 0.5 km is adopted, consistent with the lowest levels of the Goddard profiling algorithm (GPROF) products, and the independent pixel approximation (IPA) is invoked in which each $0.25^\circ \times 0.25^\circ$ pixel is treated as radiatively isolated from its neighbors. Additional details regarding the BUGSrad implementation in HERB 2008 can be found in LS03.

The HERB algorithm has recently undergone significant refinements to improve its accuracy and extend its range of applicability. The most significant of these is the extension of the algorithm to land surfaces, using a model of visible albedo and infrared emissivity that represents the characteristics of 20 different land surface types identified in the International Geosphere/Biosphere Programme (IGBP) land surface classification. A complete description of these surface types and the source of the spectral albedo curves used to define their properties can be found (available online at <http://www-surf.larc.nasa.gov/surf/pages/explan.html>) for surface types that undergo significant seasonal variations such as cropland and forested areas, separate albedo tables are adopted for summer and winter conditions, and a simple sinu-

soidal interpolation is used to determine appropriate albedos and emissivities for any day of the year. This addresses a significant shortcoming of the previous version of the approach that applied only over oceanic surfaces. In the present version, only snow-covered surfaces are not considered because of challenges in modeling their properties and retrieving overlying clouds. Although techniques exist for these purposes, the additional effort required to adapt these techniques to the VIRS instrument is not justified, given TRMM's tropical focus. Instead, variability in the visible reflectance of clear pixels on a monthly scale is used to screen potentially snow-covered surfaces. Over the course of the 10-yr TRMM dataset, less than 1% of pixels are screened for potential contamination by snow.

Clouds and rainfall over land are retrieved using similar techniques as over water, but it should be noted that the much higher emissivities of the land surface impose severe limitations on the passive microwave retrievals of low clouds and rainfall. The 2A12 product over land, for example, relies almost entirely on ice scattering at 85 GHz to infer rainfall, whereas the land-based low-cloud algorithm of Greenwald et al. (1997) that is employed in HERB exhibits a tenfold reduction in sensitivity relative to its oceanic counterpart. Furthermore, land surface emissivities exhibit significantly more variability than those over oceans, further increasing the uncertainties in liquid-cloud and rainfall retrievals. The impact of these uncertainties on the HERB flux estimates is not yet known; however, the consistent use of passive microwave radiances over both land and ocean surfaces both allows for low clouds and rainfall to be retrieved in the presence of overlying ice clouds and avoids potential day-night differences in low-cloud characteristics.

Other changes to the algorithm have centered on improving the representation of clouds and aerosols in the atmosphere. The LS03 algorithm employed a static model of the global distribution of aerosols based on annually averaged aerosol optical depths (AOD) from the Global Aerosol Climatology Project (GACP). HERB 2008, on the other hand, employs aerosol optical depth information from the Spectral Radiation-Transport Model for Aerosol Species (SPRINTARS) global aerosol transport model, which couples a model of aerosol sources and sinks with an atmospheric general circulation model (AGCM) to predict the spatial and vertical distributions of the number and mass concentrations of five aerosol species: including sulfates, sea salt, dust, organic carbon, and black carbon (Takemura et al. 2000, 2002, 2005). Direct comparison of SPRINTARS AOD with the Moderate Resolution Imaging Spectroradiometer (MODIS) level 3 daily 1° aerosol product (collection 5; Platnick et al. 2003) in cloud-free conditions (~ 7 million pixels)

indicates a bias of less than 20% and a correlation of 0.5 between the two products. This is considered acceptable, given potential uncertainties in the satellite data. The advantage to using SPRINTARS over MODIS to specify AOD is that the former applies over both land and ocean surfaces, independent of whether clouds are present. With this modification, HERB 2008 is better suited to representing variability in the tropical radiation budget caused by aerosols.

HERB 2008 also features an improved algorithm for daytime cloud detection that combines visible and infrared observations from VIRS. At solar zenith angles less than 75°, a visible reflectance greater than one standard deviation above that of the clearest pixel in the preceding month is required to indicate the presence of a cloud. Thin, high clouds that may be missed by the visible cloud mask and those occurring at night are identified by requiring that the IR brightness temperature be one standard deviation colder than the clearest pixel. Finally, low clouds at night and those residing beneath high clouds continue to be identified using an independent TMI-based cloud liquid water path retrieval, providing a more robust method for identifying these clouds than would be possible from IR measurements alone (Greenwald et al. 1993). These changes lead to more precise agreement with CERES TOA flux observations in short time scales and yield daytime cloud patterns that are more consistent with global climatologies than the LS03 version of the approach.

To date, the HERB algorithm has been applied to 10-yr of TRMM observations from January 1998 through December 2007. The product provides summaries of all cloud and atmospheric properties, surface rainfall, and the time and geolocation information used in the retrieval, as well as profiles of LW and SW fluxes and corresponding radiative heating rates at a 0.25° spatial resolution. Profile information is provided at a nominal vertical resolution of 1 km, although the true “physical” resolution of the product is likely coarser than this because of the exclusive use of passive observations for constraining cloud geometry (see later). It should also be noted that the precessing nature of TRMM’s orbit results in day-to-day changes in the local overpass time at any given location. Although this allows TRMM to sample the full diurnal cycle, it also imparts a diurnal cycle signal that dominates SW flux calculations. As a result, the HERB algorithm is run in two distinct modes. The first, designed for short-term studies, uses the true solar insolation at the time of overpass, allowing direct comparison with other satellite, ground, and model-derived fields. The other, adapted for climate-oriented studies, adopts the diurnally averaged solar insolation appropriate to the latitude and day of the year for each

TABLE 1. RMS differences (in W m^{-2}) between HERB estimates of outgoing LW radiation and collocated CERES observations on a range of time and space scales.

	Instantaneous	3-day avg	5-day avg	10-day avg	30-day avg
All surfaces					
1°	17.9	12.6	10.9	9.54	8.56
5°	15.5	9.72	8.49	7.83	6.99
10°	14.1	8.61	7.64	7.25	6.60
20°	12.9	7.63	6.86	6.67	6.23
Land only					
1°	27.2	15.7	13.0	11.4	9.57
5°	23.2	12.1	10.1	9.33	7.63
10°	20.2	10.6	8.66	8.21	6.75
20°	8.70	5.75	5.60	5.97	5.44
Ocean only					
1°	12.9	11.3	10.1	8.88	8.21
5°	10.8	8.73	8.03	7.44	6.92
10°	9.45	7.87	7.46	7.09	6.74
20°	8.14	7.10	6.88	6.73	6.60

observation. Both solutions are included in the HERB 2008 product.

3. Evaluation

a. Comparisons with CERES

Measurements of TOA fluxes by CERES provide the most straightforward means of estimating uncertainties in the HERB algorithm. The eight months of data collected by CERES on TRMM provide $\sim 3 \times 10^8$ independent observations, spanning the complete range of cloud scenes, surface types, and environmental conditions observed across the TRMM region and allow comparisons to be made on a variety of spatial and temporal averaging scales. This provides important information regarding the relative magnitudes of random and systematic errors in the HERB product.

Over the eight-month period of overlap between the two products, RMS differences between monthly-5° estimates of outgoing shortwave radiation (OSR) and outgoing longwave radiation (OLR) from HERB and CERES observations are 11 and 7 W m^{-2} respectively. During this period, the mean OSR estimated by HERB was 100 W m^{-2} , representing a bias of approximately 1 W m^{-2} higher than CERES. Similarly, HERB estimates the OLR to be 252 W m^{-2} , about 5 W m^{-2} lower than observed by CERES. Table 1 presents results for additional averaging scales summarizing RMS differences between HERB TOA LW fluxes, and those from the CERES TRMM edition 2C CRS product over spatial scales ranging from 1° to 20° and temporal scales from instantaneous to monthly. In short time scales, random

TABLE 2. As in Table 1, but for outgoing SW radiation. Differences are expressed in terms of albedo to avoid disproportionately weighting observations at low solar zenith angles.

	Instantaneous	3-day avg	5-day avg	10-day avg	30-day avg
All surfaces					
1°	0.073	0.066	0.061	0.054	0.043
5°	0.054	0.043	0.041	0.037	0.029
10°	0.042	0.036	0.034	0.030	0.024
20°	0.028	0.026	0.026	0.024	0.019
Land only					
1°	0.086	0.080	0.075	0.070	0.058
5°	0.064	0.054	0.054	0.051	0.042
10°	0.051	0.049	0.047	0.046	0.036
20°	0.038	0.039	0.047	0.042	0.035
Ocean only					
1°	0.068	0.060	0.055	0.047	0.036
5°	0.052	0.040	0.037	0.033	0.024
10°	0.040	0.033	0.030	0.027	0.021
20°	0.027	0.025	0.026	0.020	0.017

errors resulting from cloud detection and microphysical properties as well as the assumed vertical distribution of water vapor can be large, leading to RMS differences of 10–20 W m⁻² depending on the spatial resolution of interest. However, because systematic changes in radiative heating generally impact the environment on longer time scales, HERB products are likely to be most useful on time scales of 10 days or more, where RMS errors quickly average out dropping by almost a factor of 2. On still longer time scales, RMS differences in monthly/5° OLR estimates, which provide a benchmark for climate studies, are less than 7 W m⁻².

Although the current version of HERB applies over both land and ocean surfaces, it is important to note that many of the component cloud and precipitation algorithms suffer from reduced sensitivity over land backgrounds. Furthermore, the lack of reliable estimates of total column water vapor over land, remove a valuable constraint on the water vapor distribution relative to oceanic backgrounds. The impacts of these shortcomings are also examined in Table 1, where RMS differences between HERB and CERES OLR are also separated by surface type. In short-space scales, OLR differences can be more than twice as large over land as over ocean; however, uncertainties in OLR estimates over land rapidly approach those observed over oceanic regions in time scales longer than five days. Uncertainties in monthly/5° OLR estimates are, for example, only 10% larger over land than over ocean.

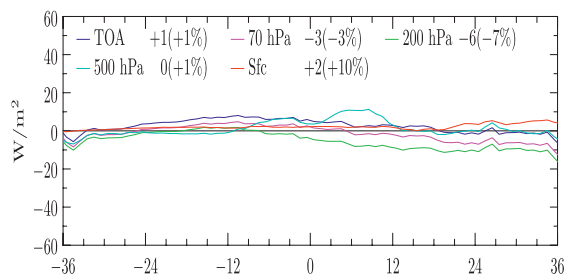
Corresponding RMS differences in OSR are summarized in Table 2. Because of the large dynamic range in SW fluxes over the diurnal cycle, OSR differences are reported in terms of pixel albedos, as opposed to abso-

lute fluxes, to avoid disproportionately emphasizing comparisons at low solar zenith angles. Uncertainties in OSR also exhibit a significant random component that reduces substantially with the averaging scale. The RMS differences at a spatial resolution of 20°, for example, are almost a factor of 3 less than those at 1° resolution. Similarly, uncertainties in monthly-mean fluxes tend to be ~40% less than those on instantaneous scales. At the benchmark resolution of monthly-5° averages, fractional uncertainties in OSR are 2.4% on the global average. In the SW, errors over land are ~50% larger than those over ocean, nearly independent of the averaging scale.

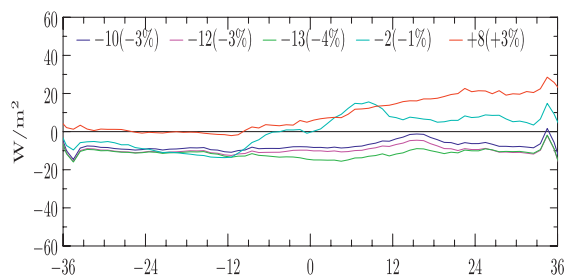
In practice, it is extremely difficult to evaluate vertically resolved atmospheric radiative fluxes and heating rates on large scales. Intercomparisons of the products of independent algorithms, however, provide a useful metric for measuring the combined uncertainties. In this case, we again turn to the CERES CRS product that also reports vertical profiles of radiative fluxes at five atmospheric levels, estimated using an approach that is similar to HERB with two major exceptions: the radiative transfer calculations are driven with cloud, aerosol, temperature, humidity, and surface property information from completely independent sources and TOA radiative fluxes are partially constrained with CERES observations (Wielicki et al. 1996). As a result of these differences, the CERES CRS and HERB products can be thought of as largely independent and comparisons between them provide a useful measure of their combined uncertainties.

Figure 1 presents differences between HERB and CERES estimates of zonally averaged up- and downwelling SW and LW fluxes at the surface, 500, 200, 70 mb, and TOA at 1° resolution for the April–August 1998 period. The higher vertical resolution HERB data are interpolated to CERES levels using log(pressure). All HERB pixels identified as having potential snow at the surface are discarded, as are data from January–March because of an error in the CERES SW algorithm over that period. Domain-averaged biases in TOA fluxes (shown in the legend) are smaller than those listed in Tables 1 and 2, suggesting additional cancellation of random errors beyond the monthly time scale. Furthermore, differences at other atmospheric levels are generally less than 4%. Two exceptions are in the downwelling LW radiation at 70 and 200 mb, where differences are on the order of 20%, indicating that the HERB atmosphere emits more LW radiation above 70 mb and less between 70 and 200 mb than the CERES atmosphere. This suggests there may be some differences in the frequency and vertical placement of thin clouds and water vapor in the upper troposphere between the algorithms; however, it should be noted that the resulting flux errors

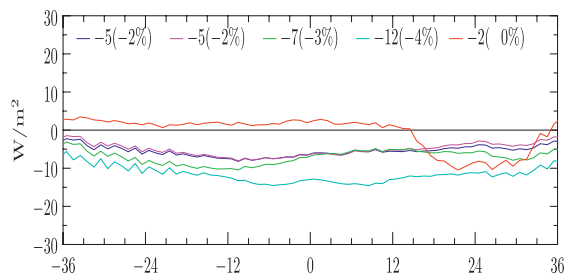
(a)



(b)



(c)



(d)

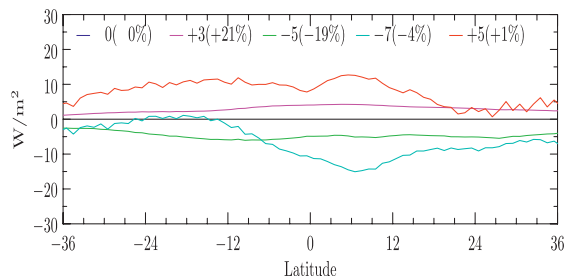


FIG. 1. Difference in zonally averaged (a) upwelling SW, (b) downwelling SW, (c) upwelling LW, and (d) downwelling LW radiative flux estimates from HERB and CERES for April–August 1998. Values in the legend represent the average bias between the products over the TRMM region expressed both in W m^{-2} and then in percent (in parentheses).

amount to less than 5 W m^{-2} in an absolute sense. Similarly, although differences in SW reflection from the surface are 10%, this amounts to a global average bias between the products of only 2 W m^{-2} .

Among the most significant features that emerge from zonal mean differences between the products are a 20 W m^{-2} surplus in downwelling SW radiation at the surface (SSR) and an $8\text{--}10 \text{ W m}^{-2}$ deficit of LW emission from the surface in the Northern Hemisphere in the HERB products relative to CERES. The surplus SSR in HERB may be an artifact of errors in cloud detection and water vapor absorption over Northern Hemisphere land surfaces, whereas differences in LW emission from the surface are indicative of slight differences in the source of surface temperature information used in each algorithm. At other levels, CERES tends to overestimate upwelling LW radiation with respect to HERB across all latitude bands, with differences getting smaller with increasing latitude. This may be a result of missing low clouds in the CERES algorithm resulting from undetected multilayered cloud systems. This is also consistent with the fact that the lower atmosphere emits more LW radiation down to the surface in the HERB algorithm, where passive microwave retrievals should allow for improved detection of liquid clouds in the presence of the overlying cirrus.

Because equatorial regions are of particular interest to many applications, comparisons between CERES and HERB flux products covering the region between 10°N and 10°S are isolated in Fig. 2. Differences exhibit increased noise relative to the zonal mean plots, because the sample size for each data point has been reduced by approximately a factor of 20. (There are now 360 one-degree longitude bins as opposed to only 72 one-degree latitude bins before. Furthermore, only 25% of the TRMM region is analyzed in Fig. 2.) Nevertheless, the overall agreement between the two products remains good, with differences rarely exceeding 5% despite the smaller area considered. LW fluxes between the surface and 500 mb once again suggest that the HERB atmosphere contains more low clouds that trap more upwelling LW radiation in the lower troposphere and emit more back down toward the surface. The meridional averages shown in Fig. 2 also reveal more pronounced features than those in the zonal plots, primarily because of differences in the treatment of land surfaces. The peaks in several fields centered at -80° and 20° , for example, correspond to the South American and African continents, respectively, whereas, large differences in downwelling SW radiation at 500 mb and the surface from $60^\circ\text{--}180^\circ$ can be attributed to the moist Indian and west Pacific Ocean regions.

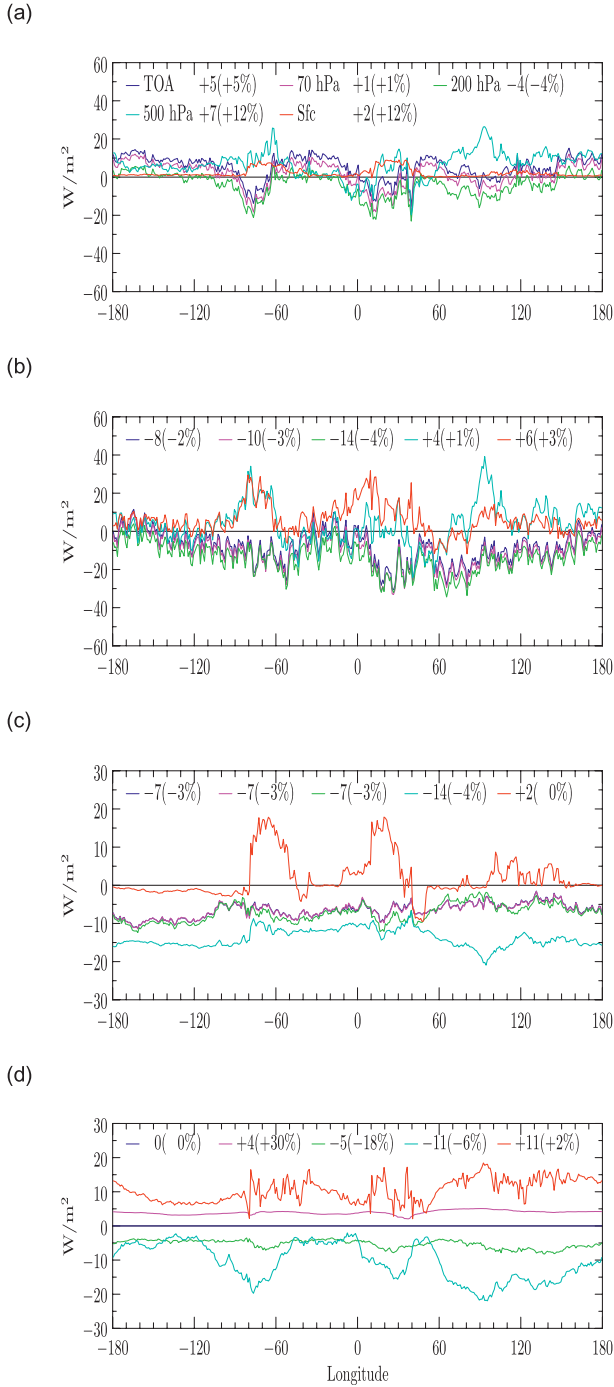


FIG. 2. As in Fig. 1, but for meridionally averaged fluxes between 10°N and 10°S .

b. Comparisons with the surface sites

HERB products are also evaluated against the CERES/ARM Validation Experiment (CAVE) collection of surface flux observations that includes regular measurements from several sites located throughout the world (Rutan et al. 2001). These sites are operated by the Department

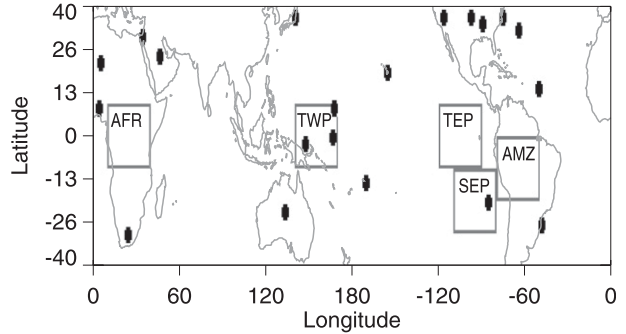


FIG. 3. Geographic distribution of surface radiation measurement sites used to evaluate HERB surface flux estimates. Boxes overlaid on the figure define regions for more detailed examination in section 5.

of Energy (DOE) ARM Program, World Climate Research Program (WCRP) Baseline Surface Radiation Network (BSRN; Ohmura et al. 1998), National Oceanic and Atmospheric Administration (NOAA) Global Baseline Sites [GMD; formerly the Climate Monitoring and Diagnostics Laboratory, (CMDL)], NOAA GMD Surface Radiation Network (SURFRAD; Augustine et al. 2000), the Woods Hole Oceanographic Institute (WHOI; Anderson et al. 2000), and a number of other independent operators. Although the CAVE dataset does not provide a true global evaluation of satellite products, the 39 ground sites and 2 buoys that lie in the TRMM domain sample several distinct environments, ranging from the Southern Great Plains (SGP) region of the United States to the tropical west Pacific (TWP). The locations of all surface sites used in this comparison are summarized in Fig. 3. It should be noted, however, that 21 of the sites examined fall within a $4^{\circ} \times 4^{\circ}$ box around the ARM SGP site.

The primary drawback to using surface observations is that they are point measurements that cannot be considered to be generally representative of the much larger 0.25° HERB resolution or the nominal nadir CERES field of view (FOV) of ~ 10 km. To crudely compensate for this effect, the three 15-min mean surface observations that are closest to the observation time of the appropriate 0.25° HERB pixel are combined into a single 45-min average, which should be more representative of cloud advection across the HERB pixel. At the same time, several CERES CRS footprints fall within a single HERB pixel. The mean of these footprints is taken and assigned the time of the associated HERB pixel, yielding three time series for each ground site: the averaged surface flux observations, HERB flux estimates, and CERES flux estimates all coregistered in space and time and each with a single value for each satellite overpass. Even with this averaging, however, significant sampling differences can exist between the three sets of fluxes because of the large differences in their effective fields of view. As a result, the

TABLE 3. Statistical summary of comparisons between HERB surface LW flux estimates and measurements at 39 ground sites and 2 buoys. Similar comparisons of CERES CRS flux products over the ensemble of all sites are included in the last row for reference.

Ground site	Lat°	Lon°	Bias (W m^{-2})	Bias (%)	RMS (W m^{-2})	Correlation
ARM, SGP central facility	36.60	-97.48	-5.00	-1.54	38.41	0.86
ARM, Darwin, AU	-12.43	130.89	-6.97	-1.76	14.36	0.92
ARM, Larned, KS	38.20	-99.32	6.75	2.08	41.31	0.84
ARM, Hillsboro, KS	38.31	-97.30	7.01	2.12	45.20	0.81
ARM, LeRoy, KS	38.20	-95.60	-7.58	-2.35	40.30	0.85
ARM, Plevna, KS	37.95	-98.33	1.88	0.58	41.30	0.84
ARM, Halstead, KS	38.11	-97.51	0.50	0.15	41.87	0.84
ARM, Towanda, KS	37.84	-97.02	10.41	3.10	48.25	0.80
ARM, Elk Falls, KS	37.38	-96.18	0.74	0.22	45.80	0.82
ARM, Coldwater, KS	37.33	-99.31	6.80	2.07	43.77	0.83
ARM, Ashton, KS	37.13	-97.27	0.88	0.27	44.12	0.83
ARM, Tyro, KS	37.07	-95.79	-8.54	-2.63	40.03	0.86
ARM, Byron, OK	36.88	-98.29	-6.18	-1.90	39.60	0.86
ARM, Pawhuska, OK	36.84	-96.43	8.99	2.64	50.91	0.79
ARM, Lamont, OK	36.60	-97.48	-11.27	-3.46	39.12	0.86
ARM, Ringwood, OK	36.43	-98.28	-1.55	-0.47	42.61	0.84
ARM, Vici, OK	36.07	-99.20	15.43	4.52	46.86	0.81
ARM, Morris, OK	35.69	-95.89	-7.47	-2.15	55.46	0.71
ARM, Meeker, OK	35.56	-96.99	4.46	1.30	42.32	0.83
ARM, Cordell, OK	35.35	-98.98	11.09	3.21	44.63	0.82
ARM, Cyril, OK	34.88	-98.20	25.99	7.17	59.14	0.75
ARM, Manus	-2.06	147.43	2.54	0.60	31.41	0.21
ARM, Nauru	-0.52	166.92	15.82	3.62	23.19	0.54
ARM, Niamey, Niger	13.48	2.18	-9.71	-2.73	34.92	0.72
BSRN, Alice Springs, Australia	-23.70	133.87	19.61	5.35	55.96	0.63
BSRN, De Aar, South Africa	-30.67	24.00	-7.91	-2.58	34.71	0.82
BSRN, Florianapolis, Brazil	-27.47	-48.48	-22.92	-6.28	39.97	0.62
BSRN, Sede Boqer, Israel	30.87	34.77	13.41	3.98	54.77	0.45
BSRN, Saudi Solar Village	24.91	46.41	2.19	0.63	52.95	0.48
BSRN, Tamanrasset, Algeria	22.78	5.52	16.11	4.71	63.77	0.53
BSRN, Tateno, Japan	36.05	140.13	13.53	3.89	54.39	0.72
COVE,* Chesapeake Lighthouse	36.90	-75.71	-8.40	-2.62	25.71	0.91
GMD, Bermuda	32.30	-64.77	20.88	5.26	41.63	0.59
GMD, Kwajalein	8.72	167.72	12.56	2.89	22.51	0.49
GMD, Mauna Loa, HI	19.54	-155.58	181.65	43.44	189.15	0.12
GMD, Samoa	-14.23	-170.56	13.80	3.18	24.53	0.41
SURFRAD, Desert Rock, NV	36.63	-116.02	-18.58	-6.54	44.72	0.77
SURFRAD, Goodwin Creek, MS	34.25	-89.87	-13.70	-4.10	36.91	0.86
NTAS,** Buoy I	14.50	-51.00	11.81	2.84	29.39	0.31
NTAS,** Buoy II	14.50	-51.00	6.65	1.60	28.22	0.33
Stratus, Buoy I	-20.20	-85.20	1.42	0.37	29.22	0.68
Stratus, Buoy II	-20.20	-85.20	16.29	4.23	31.92	0.73
Stratus, Buoy III	-20.20	-85.20	6.43	1.65	29.50	0.67
All sites: HERB	—	—	3.28	0.95	44.23	0.82
All sites: CERES	—	—	-1.72	-0.48	18.37	0.95

* CERES Ocean Validation Experiment.

** Northwest Tropical Atlantic Station.

focus of the comparisons that follow is slanted towards long-term biases between calculated and measured surface fluxes rather than RMS errors between them.

Comparisons of the full 10-yr HERB dataset with all 39 surface stations and both WHOI buoys are summarized in Tables 3 and 4. The mean statistics for CERES from all sites are also summarized in the last row for comparison, although these comparisons only span the

period over which CERES was operational. Again, biases are reported both in W m^{-2} and as percentages to account for the much larger dynamic range of SSR at each site (and between sites) than downwelling LW radiation at the surface (SLR). The impact of the large spatial scale of the HERB observations is immediately evident in comparisons against surface observations at Mauna Loa. The 0.25° resolution of the HERB product is too large to

TABLE 4. As in Table 3, but for downwelling SW fluxes at the surface.

Ground site	Lat°	Lon°	Bias (W m^{-2})	Bias (%)	RMS (W m^{-2})	Correlation
ARM, SGP central facility	36.60	-97.48	41.17	17.66	110.63	0.95
ARM, Darwin, AU	-12.43	130.89	55.75	19.25	145.67	0.94
ARM, Larned, KS	38.20	-99.32	35.60	15.65	97.68	0.96
ARM, Hillsboro, KS	38.31	-97.30	31.78	14.61	95.16	0.96
ARM, LeRoy, KS	38.20	-95.60	44.71	19.86	111.53	0.95
ARM, Plevna, KS	37.95	-98.33	39.80	17.43	103.76	0.95
ARM, Halstead, KS	38.11	-97.51	38.45	17.01	101.87	0.95
ARM, Towanda, KS	37.84	-97.02	34.57	15.76	103.42	0.95
ARM, Elk Falls, KS	37.38	-96.18	38.85	18.57	107.28	0.94
ARM, Coldwater, KS	37.33	-99.31	34.36	15.27	98.00	0.96
ARM, Ashton, KS	37.13	-97.27	37.09	16.54	102.77	0.95
ARM, Tyro, KS	37.07	-95.79	40.79	18.57	109.98	0.94
ARM, Byron, OK	36.88	-98.29	38.94	16.96	103.13	0.96
ARM, Pawhuska, OK	36.84	-96.43	29.01	14.70	106.42	0.94
ARM, Lamont, OK	36.60	-97.48	42.72	18.44	111.12	0.95
ARM, Ringwood, OK	36.43	-98.28	36.61	16.12	102.21	0.95
ARM, Vici, OK	36.07	-99.20	31.43	14.06	96.78	0.96
ARM, Morris, OK	35.69	-95.89	33.06	16.23	107.67	0.94
ARM, Meeker, OK	35.56	-96.99	36.20	16.78	106.90	0.95
ARM, Cordell, OK	35.35	-98.98	33.79	14.64	100.25	0.96
ARM, Cyril, OK	34.88	-98.20	20.61	10.18	100.32	0.94
ARM, Manus	-2.06	147.43	43.72	17.04	143.02	0.92
ARM, Nauru	-0.52	166.92	23.87	9.36	109.08	0.95
ARM, Niamey, Niger	13.48	2.18	31.52	11.23	71.81	0.99
BSRN, Alice Springs, Australia	-23.70	133.87	0.00	-0.00	-999.00	-999.00
BSRN, De Aar, South Africa	-30.67	24.00	25.12	9.48	89.15	0.97
BSRN, Florianopolis, Brazil	-27.47	-48.48	61.97	25.28	155.64	0.91
BSRN, Sede Boquer, Israel	30.87	34.77	18.55	7.28	86.02	0.97
BSRN, Saudi Solar Village	24.91	46.41	27.10	9.48	68.29	0.99
BSRN, Tamanrasset, Algeria	22.78	5.52	20.04	6.82	86.51	0.97
BSRN, Tateno, Japan	36.05	140.13	44.26	21.50	128.87	0.91
COVE, Chesapeake Lighthouse	36.90	-75.71	39.16	17.85	99.27	0.96
GMD, Bermuda	32.30	-64.77	23.69	11.23	105.06	0.94
GMD, Kwajalein	8.72	167.72	12.89	5.36	96.99	0.96
GMD, Mauna Loa, HI	19.54	-155.58	-31.83	-12.13	128.37	0.95
GMD, Samoa	-14.23	-170.56	23.91	9.84	107.90	0.95
SURFRAD, Desert Rock, NV	36.63	-116.02	25.54	9.87	81.20	0.98
SURFRAD, Goodwin Creek, MS	34.25	-89.87	51.27	22.25	121.94	0.94
NTAS, Buoy I	14.50	-51.00	18.71	6.82	83.21	0.97
NTAS, Buoy II	14.50	-51.00	19.61	7.11	106.12	0.95
Stratus, Buoy I	-20.20	-85.20	17.16	7.96	87.17	0.96
Stratus, Buoy II	-20.20	-85.20	-0.24	-0.11	92.52	0.95
Stratus, Buoy III	-20.20	-85.20	5.44	2.69	95.69	0.95
All sites: HERB	—	—	34.09	14.99	105.25	0.95
All sites: CERES	—	—	17.48	6.34	61.81	0.98

capture the extreme elevation of the mountain site and, as a result, HERB overestimates SLR (Table 3) by more than 180 W m^{-2} and underestimates SSR by nearly 40 W m^{-2} (Table 4) relative to the surface observations. These overestimates in emission and absorption in the lower atmosphere also exist in CERES downwelling flux estimates at the Mauna Loa site. Given these obvious differences in atmospheric properties, owing to sampling volume differences between the satellite and ground site, the Mauna Loa data are excluded from the overall statistics summarized in the last row of each table.

The average bias in HERB SLR over all sites is less than 4 W m^{-2} , consistent with comparisons against CERES TOA LW fluxes. Biases at individual sites can, however, exceed 20 W m^{-2} or 6%, but biases vary significantly from site to site, pointing to potential sample volume issues as a possible explanation for these errors. Elk Falls and Towanda, Kansas, for example, are separated by a single HERB pixel but exhibit biases of -5 and 23 W m^{-2} , respectively. This reflects the fact that neither the surface nor atmospheric property models used in HERB can represent finescale structure in topography,

vegetation, inland water bodies, and land use and suggests that HERB products are better suited to somewhat larger time and space scales. Correlations between HERB SLR estimates and surface observations are generally good (~ 0.8 on average) but are smaller than those for SSR estimates because of the relatively small dynamic range of SLR over some sites, emphasizing the impact of large random errors resulting from cloud inhomogeneity over the large HERB pixels.

Both the CERES and the HERB products significantly overestimate downwelling SW radiation at the surface, although biases in the HERB product are nearly twice as large as those in the CERES. These biases may be partially explained by absorption from trace gas species, such as methane, which are not included in the correlated- k treatment presently adopted in HERB; however, comparisons with the MSTRNX model (Sekiguchi and Nakajima 2008), which includes a more complete trace gas inventory, suggest that the resulting biases are generally $\sim 5 \text{ W m}^{-2}$ or less. The source of the remaining bias requires further investigation but can likely be attributed to a combination of uncertainties in aerosol scattering properties, the lack of an observation-based constraint on column water vapor over land, errors in cloud detection over brighter land surfaces, and the effects of cloud inhomogeneity within the CERES and even larger HERB FOVs. Cloud, aerosol, and surface properties in the HERB product, for example, are assumed to be homogeneous across each 0.25° pixel, leading to not only large random errors on a pixel-by-pixel basis but also having potential impacts on cloud detection and microphysical property retrievals that are based on pixel mean radiances. This is consistent with the large RMS differences in both SLR and SSR and with the fact that CERES fluxes exhibit somewhat smaller uncertainties, because CERES footprints cover an area of $\sim 100 \text{ km}^2$, which is 6 times smaller than the 625 km^2 area of a HERB pixel. Furthermore, all of the component algorithms in HERB have greater sensitivity to clouds and precipitation over oceanic regions, where few surface flux datasets exist for comparison. This is supported by the fact that HERB SSR estimates show much better overall agreement at the GMD Kwajalein site and the WHOI buoys that are the most representative of oceanic pixels in the satellite retrievals.

Assuming the source of the biases can be determined through further investigation, correlations between HERB and measured SSR are greater than 0.95 for all sites, suggesting that the bias between them is reasonably stationary. This, coupled with the fact that similar biases exist over all land-based surface radiation sites, indicates that the dataset may resolve changes in SSR over time and relative differences between regions that are smaller

than the overall biases in the product. This is emphasized in Fig. 4, where comparisons of multiyear time series of downwelling LW and SW flux anomalies are presented for the ARM sites at Nauru and Byron (part of the SGP network). The data have been averaged to a 46-day resolution to remove the diurnal cycle imposed by TRMM's precessing orbit. Once biases have been removed, the agreement between HERB flux estimates and those observed at each ground site is generally very good. Beyond capturing the seasonal cycle of SW and LW radiation incident at the surface at the ARM site, HERB also captures year-to-year variations resulting from changes in cloud cover and precipitation. For example, HERB captures the slower than normal increase in SSR associated with the wetter than normal spring of 2006 at the Byron site and the subsequent broader than normal SSR maximum associated with drought conditions in 2007 (X. Dong et al. 2009, unpublished manuscript). Although surface fluxes are less variable at Nauru because of its tropical location, HERB captures the vast majority of the oscillations in observed SSR, because of transient features such as MJO events. Downwelling LW fluxes at Nauru are least variable of all, resulting from the nearly constant humidity and surface temperature, but even here HERB captures a slow interannual modulation of SLR that is likely attributable to the El Niño–Southern Oscillation (ENSO). The observed variations correlate very well with the NOAA multivariate ENSO index (MEI), showing a distinct reduction in SLR during periods of negative MEI (La Niña; e.g., 2000/01 and 2006) and enhanced SLR during positive MEI episodes (El Niño; e.g., late 2002, 2005, and 2007).

Beyond supplying a baseline estimate of the accuracy of the HERB flux estimates, this evaluation of TOA and SFC fluxes can be used to provide a crude measure of the expected accuracy of atmospheric heating rates. Noting that atmospheric radiative heating is related to radiative flux convergence through $Q = (g/c_p)(dF/dp)$, where c_p is the specific heat at constant pressure, estimates of the uncertainties in fluxes at the atmospheric boundaries can be used to provide an upper bound on the uncertainty in atmospheric radiative heating. For example, based on Table 1, RMS errors in monthly- 5° outgoing LW and SW fluxes at TOA are 7 and 11 W m^{-2} , respectively, assuming a diurnally averaged solar insolation of 380 W m^{-2} . Similarly, the surface flux comparisons suggest monthly errors in LW and SW fluxes on the order of 4 and 34 W m^{-2} , respectively, based on the overall comparisons against all ground observation sites presented in Tables 3 and 4. If it is assumed that the uncertainties in TOA and SFC fluxes are uncorrelated, then the implied uncertainties in HERB column atmospheric heating rates are $\delta Q_{\text{LW}} = 0.09 \text{ K day}^{-1}$ and $\delta Q_{\text{SW}} = 0.36 \text{ K day}^{-1}$.

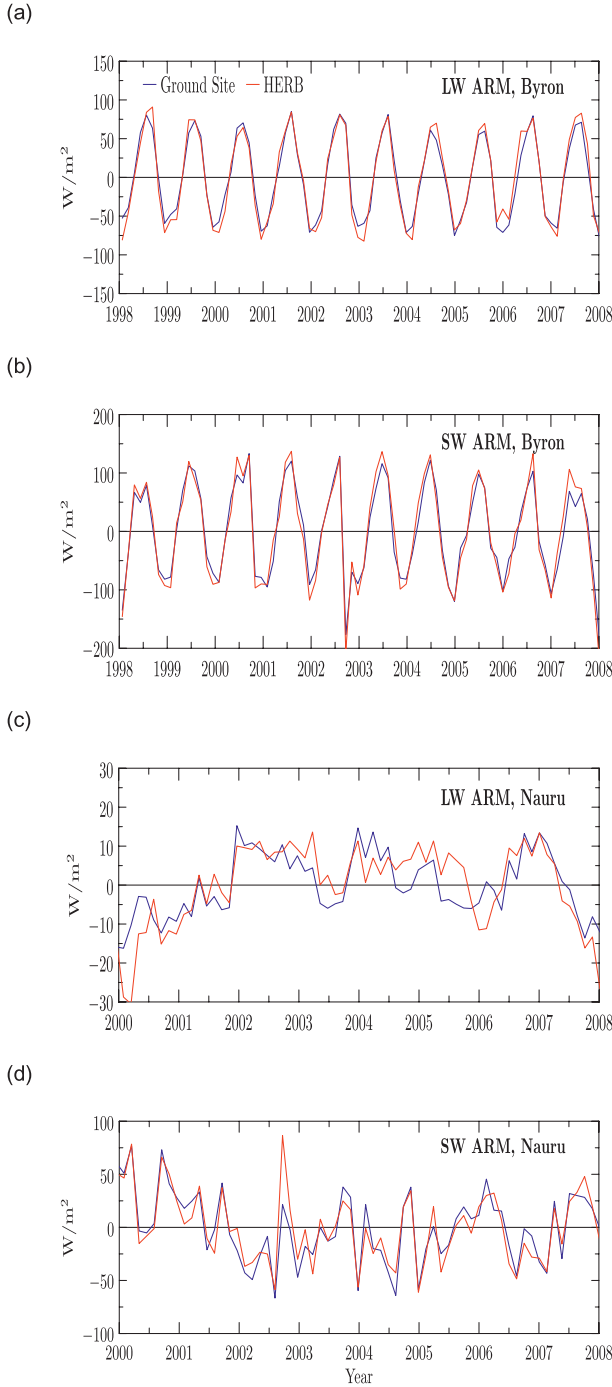


FIG. 4. Anomaly time series of downwelling LW and SW fluxes from HERB and the ARM surface radiation sites at (a),(b) Byron, Oklahoma, and (c),(d) Nauru. LW fluxes are reported in (a) and (c), whereas SW fluxes are reported in (b) and (d). In all cases, 46-day averages are displayed to remove the diurnal sampling effects of TRMM's precessing orbit and the means from each dataset have been removed.

The tropical mean is $Q_{\text{LW}} \sim -1.6 \text{ K day}^{-1}$ and $Q_{\text{SW}} \sim 0.6 \text{ K day}^{-1}$, which suggests errors of approximately 6% in LW heating estimates and 60% in SW heating estimates at a monthly-5° resolution. Note, however, that δQ_{SW} is likely overestimated in this simple analysis, because errors in cloud impacts on SW fluxes at TOA and SFC tend to be strongly correlated. In reality, these uncertainties depend strongly on time and the spatial averaging scale; however, this provides a rough estimate for establishing the significance of the results that follow.

4. Radiative properties of the tropical and subtropical atmospheres

Figure 5 shows the 10-yr mean radiation budget at TOA and SFC (defined as positive in the downward direction) and the corresponding atmospheric flux divergence across the TRMM region that represents approximately two-thirds of the globe. Strong year-round solar insolation dominates the TOA radiation budget in the tropics, exceeding the combined outgoing LW and SW radiation by nearly 100 W m^{-2} over large portions of the tropical Pacific and Indian oceans. When compared with the associated climatologies of surface and atmospheric properties for the same period, which are summarized in Fig. 6, it is clear that the strongest net TOA radiation imbalances are driven by the trapping of LW radiation by high clouds associated with deep convection. Furthermore, these regions strongly correlate with areas of mean large-scale ascent, based on NCEP reanalysis consistent with Bony et al. (2004) and Yuan et al. (2008), who note a strong connection between the abundance of high clouds, their impact on outgoing LW radiation, and vertical motion. In neighboring regions where high clouds are less prevalent, such as the east Pacific, energy imbalances at TOA are $20\text{--}30 \text{ W m}^{-2}$ less than in the west Pacific. Surplus radiation at TOA decreases strongly with increasing latitude outside the tropics because of the reduced solar insolation in winter seasons but remains positive over most of the TRMM domain. The often cloud-free desert regions provide the unique exception, losing approximately 20 W m^{-2} to space resulting from very strong OLR and enhanced surface reflection from the bright desert surface.

Throughout the TRMM region, there is generally a strong net surplus of radiation at the surface because of the combination of downwelling SW radiation and atmospheric emission to the surface, which exceeds its LW emission by $100\text{--}200 \text{ W m}^{-2}$ over the entire region. Net surface radiation imbalances are largest in subsidence regions near the equator, such as the east Pacific and Atlantic, where more of the strong solar insolation reaches the surface resulting from the reduced cloud cover relative

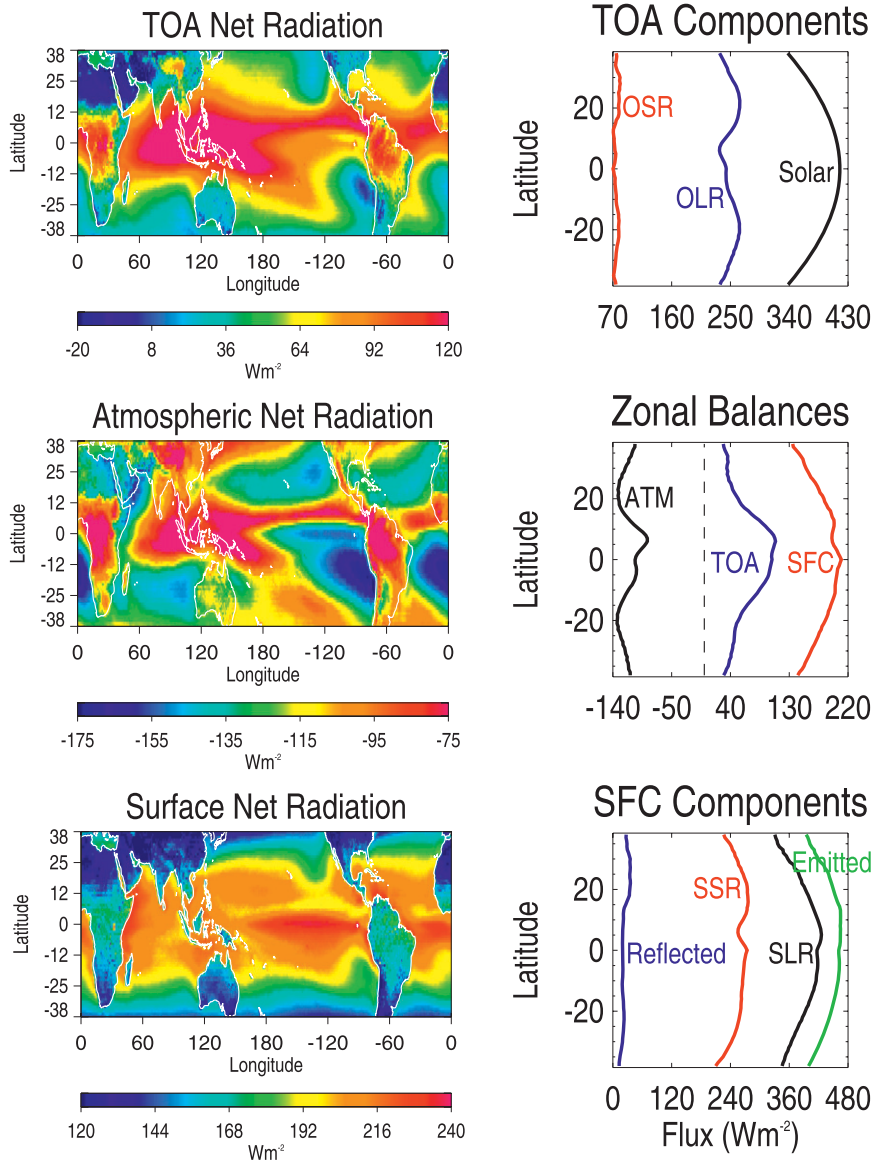


FIG. 5. (left) The 10-yr mean net radiation balance at the top of the atmosphere, within the atmosphere, and at the surface and the (right) zonal averages of the contributing fluxes are presented.

to the convergence zones. Brighter surfaces coupled with reduced emission from drier atmospheres lead to notably smaller net surface radiation imbalances over land surfaces, especially over desert regions. This land-ocean contrast in the surface radiation budgets is further enhanced by continental convection in the Amazon and Congo regions.

The difference between the net TOA and SFC energy radiation budgets provides an estimate of the total atmospheric radiative flux divergence Q_R . Here, Q_R exhibits the strongest contrasts between regions of large-scale ascent and subsidence with more than twice as much cooling

in the latter resulting from the combination of less excess radiation at TOA and the strongest net surplus of radiation to the surface. These differences are primarily driven by changes in cloud characteristics, with high clouds closely correlating with areas of large-scale ascent significantly reducing LW cooling, whereas persistent low-level cloudiness in areas of subsidence act to increase it. In fact, the map of atmospheric flux divergence qualitatively correlates more closely with NCEP vertical motion than it does with SST, illustrating the strong mutual connection between atmospheric dynamics, cloud morphology, and radiative flux divergence on

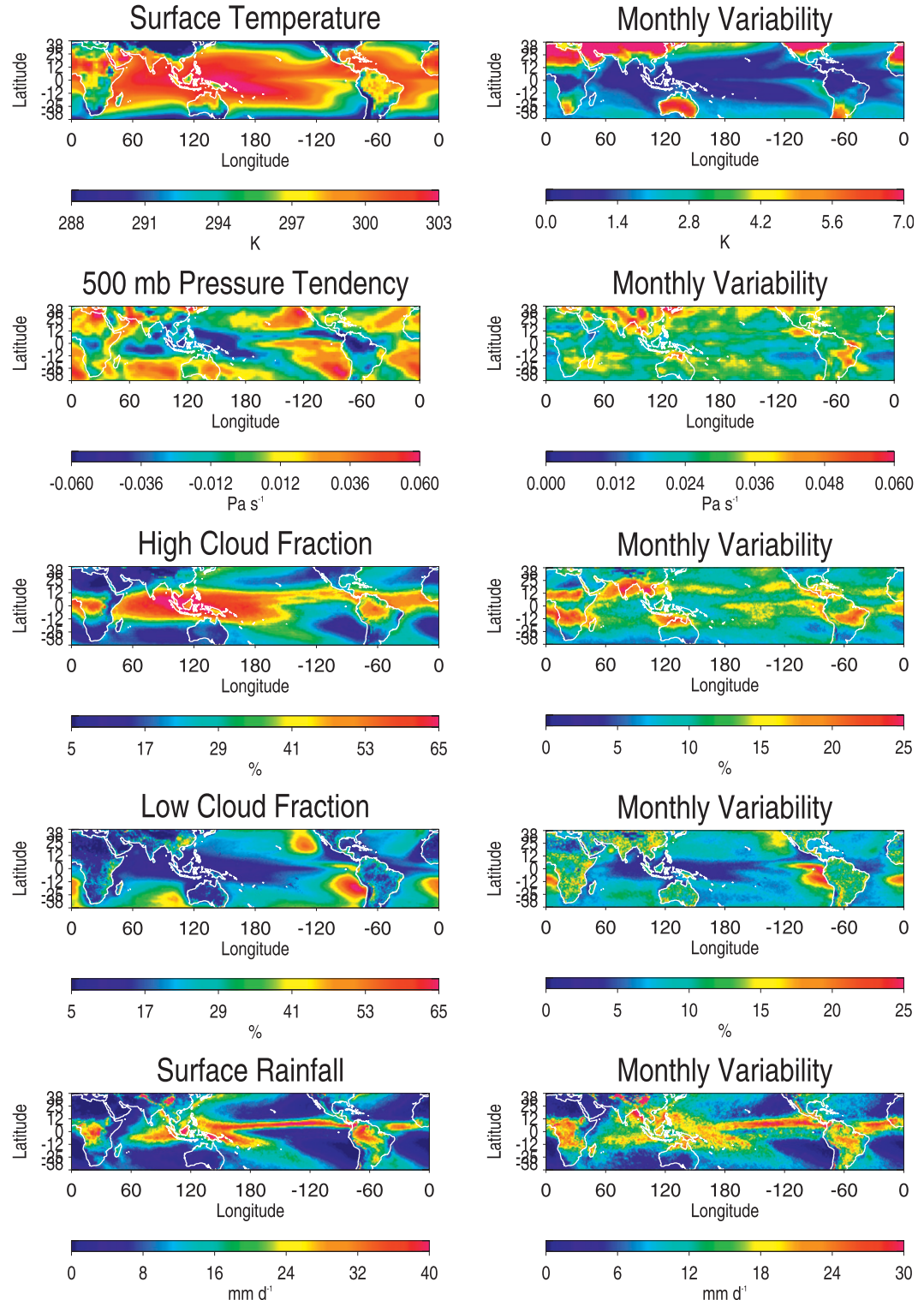


FIG. 6. (left) The 10-yr mean surface temperature, 500-mb vertical air motion, high- and low-cloud fraction, and surface rainfall. All parameters are retrieved from the TRMM sensors, with the exception of vertical air motion, which is from NCEP reanalyses. High clouds consist of all clouds that pass the VIRS-based ice-cloud screen, whereas low clouds are defined as those with nonzero TMI LWP. (right) The month-to-month variability in each field is presented.

the large scale. When combined with the latitude dependence of solar insolation, zonal variations in high- and low-cloud amounts associated with vertical motion result in a slightly asymmetric zonal distribution of atmospheric radiative cooling, with distinct peaks at 20°N and 20°S, where subsidence is strongest.

5. Vertical distribution of Q_R

The 10-yr mean of net column-integrated atmospheric radiative cooling in the HERB dataset is -1.14 K day^{-1} , and differences between convectively active regions and areas of persistent subsidence lead to deviations of $\pm 0.45 \text{ K day}^{-1}$ from this average. Given the sensitivity of the vertical profile of atmospheric radiative heating $Q_R(z)$ to cloud boundaries, water vapor scale height, and the atmospheric temperature profile, the most significant regional gradients in atmospheric heating are generally confined to narrower vertical layers. Furthermore, it is the vertical distribution of radiative heating rather than its column integral that is likely to impart the strongest influence on atmospheric dynamics.

a. Spatial distribution

Toward the goal of quantifying regional differences in the vertical structure of atmospheric radiative heating within the TRMM region, Q_{SW} and Q_{LW} across four coarse vertical layers are summarized in Figs. 7–8 revealing striking differences in the factors governing LW and SW heating at different levels in the atmosphere. Regional differences in SW heating exhibit a clear transition from being dominated by clouds at the upper and lower levels and water vapor in between. The distribution of Q_{SW} between 12 and 20 km, for example, resembles a map of high-cloud fraction while between the surface and 2-km trace regions of persistent low cloudiness. SW heating maps between 2 and 12 km resemble those of 500-mb vertical motion, whereas cloud impacts, defined as all-sky minus clear-sky Q_{SW} , account for less than 10% of the total SW heating. This suggests that regional differences in Q_{SW} can be attributed instead to regional variations in water vapor scale height. In regions of ascending motion, SW heating is spread over a deeper column that extends into the 5–12-km layer, whereas SW heating in subsidence regions tends to be confined to the 2–5-km layer. The only evidence of enhanced SW heating by clouds between 2 and 5 km is confined to small regions of very persistent stratocumulus near the west coasts of North and South America and Africa.

The column-integrated impact of clouds on column SW heating is generally small but exhibits a distinct pattern indicating that low clouds consistently increase

column Q_{SW} , whereas high clouds tend to reduce it (Fig. 7, top right). This pattern is particularly evident over ocean regions and can be entirely attributed to additional reflection by clouds relative to the much darker ocean surface. Radiation reflected by low clouds effectively experiences twice as much water vapor path above cloud, allowing significantly more absorption. High clouds, on the other hand, decrease the amount of SW radiation that reaches the lower troposphere, in turn reducing absorption at lower levels. Although these effects are generally small, they are persistent and can account for $\sim 10\%$ of the annual mean total column SW heating.

LW cooling (Fig. 8) tends to peak in the layer between 5 and 12 km, with the strongest cooling occurring in the east Pacific. Heating by high clouds reduces the strength of peak LW cooling by as much as 0.5 K day^{-1} in areas of frequent convection, such as the west Pacific, Amazon, and Congo. The effects of high clouds are also evident at lower levels, where water vapor emission is reduced in the presence of enhanced downwelling LW radiation from high clouds (Tian and Ramanathan 2002). Conversely, in regions of very strong subsidence, a lack of high clouds coupled with strong emission to the surface from low clouds leads to a secondary maximum in LW cooling in the layer below 2 km. Finally, it is worth noting that upper-tropospheric water vapor also plays an important role in the regional distribution of radiative cooling between 12 and 20 km. Here a combination of cloud-top cooling and enhanced water vapor emission can lead to significant LW cooling in regions of strong convergence, while surrounding regions experience minimal cooling in this layer. This has potentially important implications for the height and strength of the tropical tropopause layer (TTL; e.g., Feldman et al. 2008).

Net atmospheric radiative heating in each layer, given by the combination of Q_{SW} and Q_{LW} , is presented in Fig. 9. Between 12 and 20 km, the enhanced LW cooling from upper-tropospheric water vapor is largely offset by the significant SW heating by high clouds in the convergence zones. The larger spatial extent of high clouds on either side of the strongest ascending motions, however, produces residual SW heating in this layer, particularly in the central and west Pacific and northern Indian oceans. Outside the tropics, where the tropopause is lower, LW cooling by CO₂ becomes significant in this layer, leading to a net cooling of 0.35 K day^{-1} . The regional structure of Q_{NET} between 5 and 12 km forms a somewhat complicated mosaic that represents the combination of cloud impacts on LW cooling and SW absorption by water vapor. The result is a strong east–west gradient in net radiative cooling in the tropical Pacific that is a factor of 2 stronger in the east. In the west Pacific, there is also a strong zonal gradient in radiative

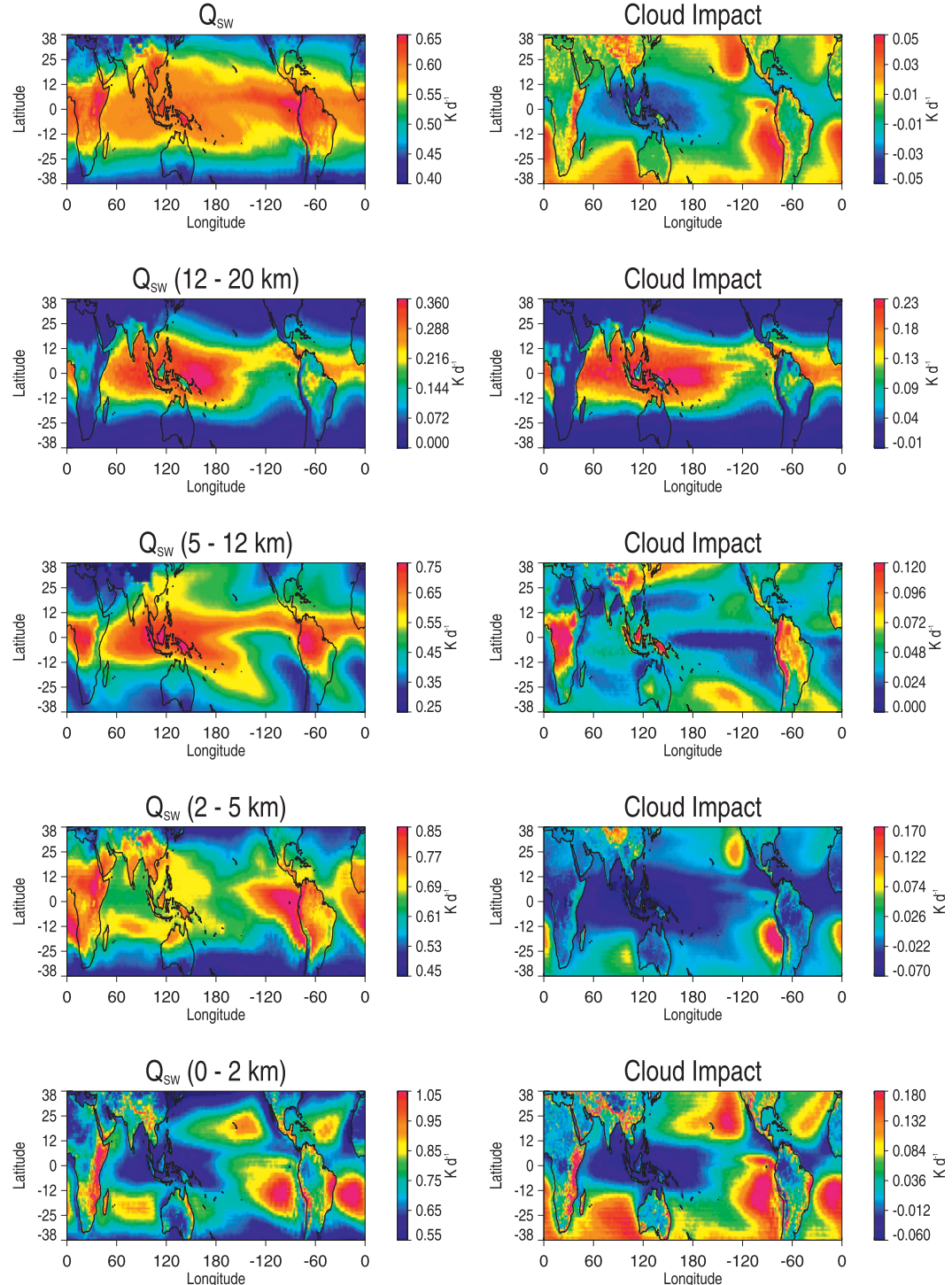


FIG. 7. (left) The 10-yr mean column-integrated shortwave atmospheric radiative heating in the TRMM region and its breakdown into four coarse atmospheric layers from the surface to 2, 2–5, 5–12, and 12 km to the tropopause. (right) Cloud impact on shortwave heating is summarized.

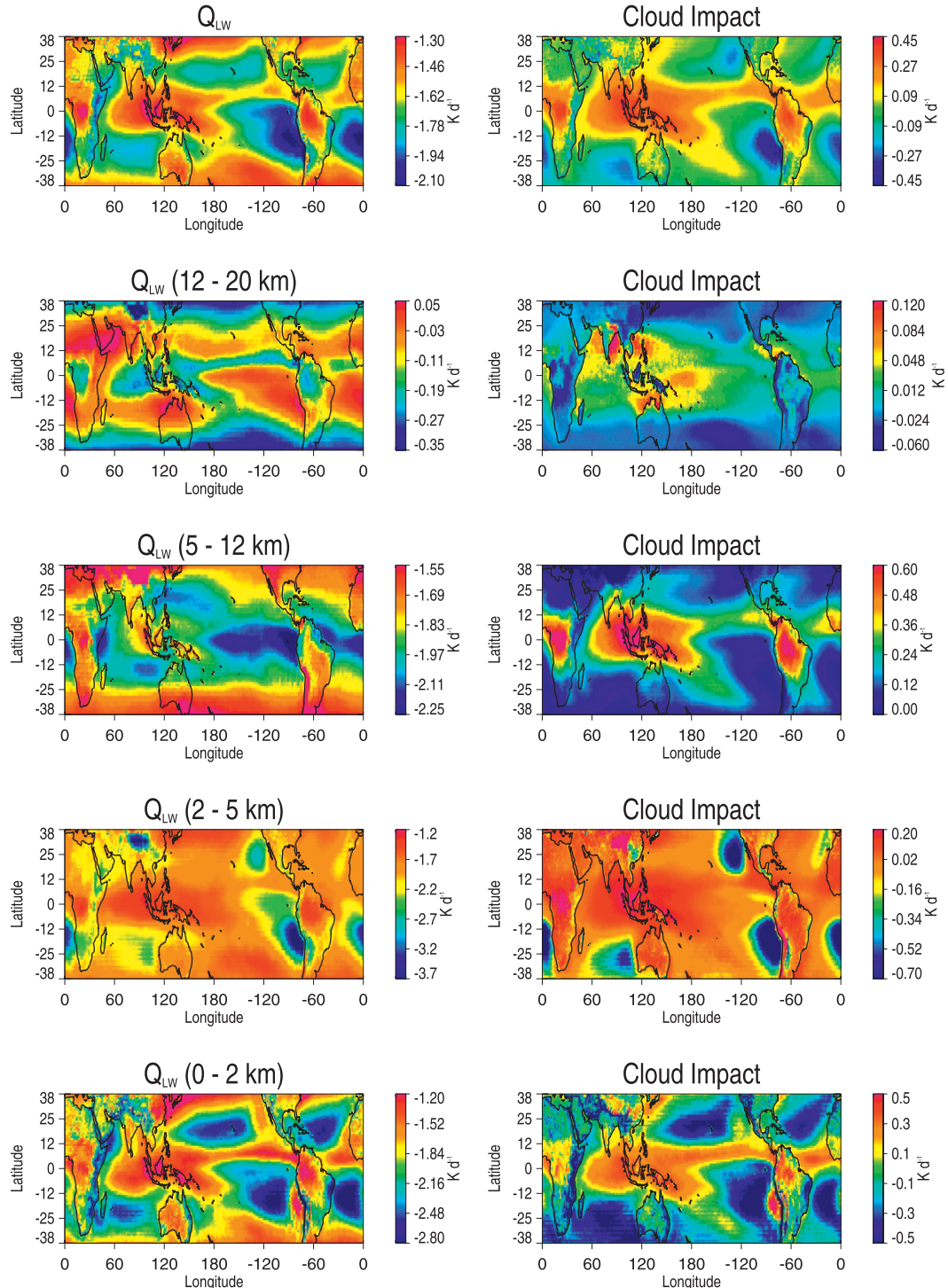


FIG. 8. As in Fig. 7, but for longwave atmospheric heating.

cooling that is $\sim 50\%$ stronger between 10° and 20° than between $\pm 10^\circ$. At lower levels, Q_{LW} covers a significantly wider dynamic range than Q_{SW} and net atmospheric radiative heating exhibit patterns that more

closely resemble those in Fig. 8. The fact that regional anomalies in SW heating are nearly anticorrelated with those in LW cooling, however, reduces regional gradients in Q_{NET} .

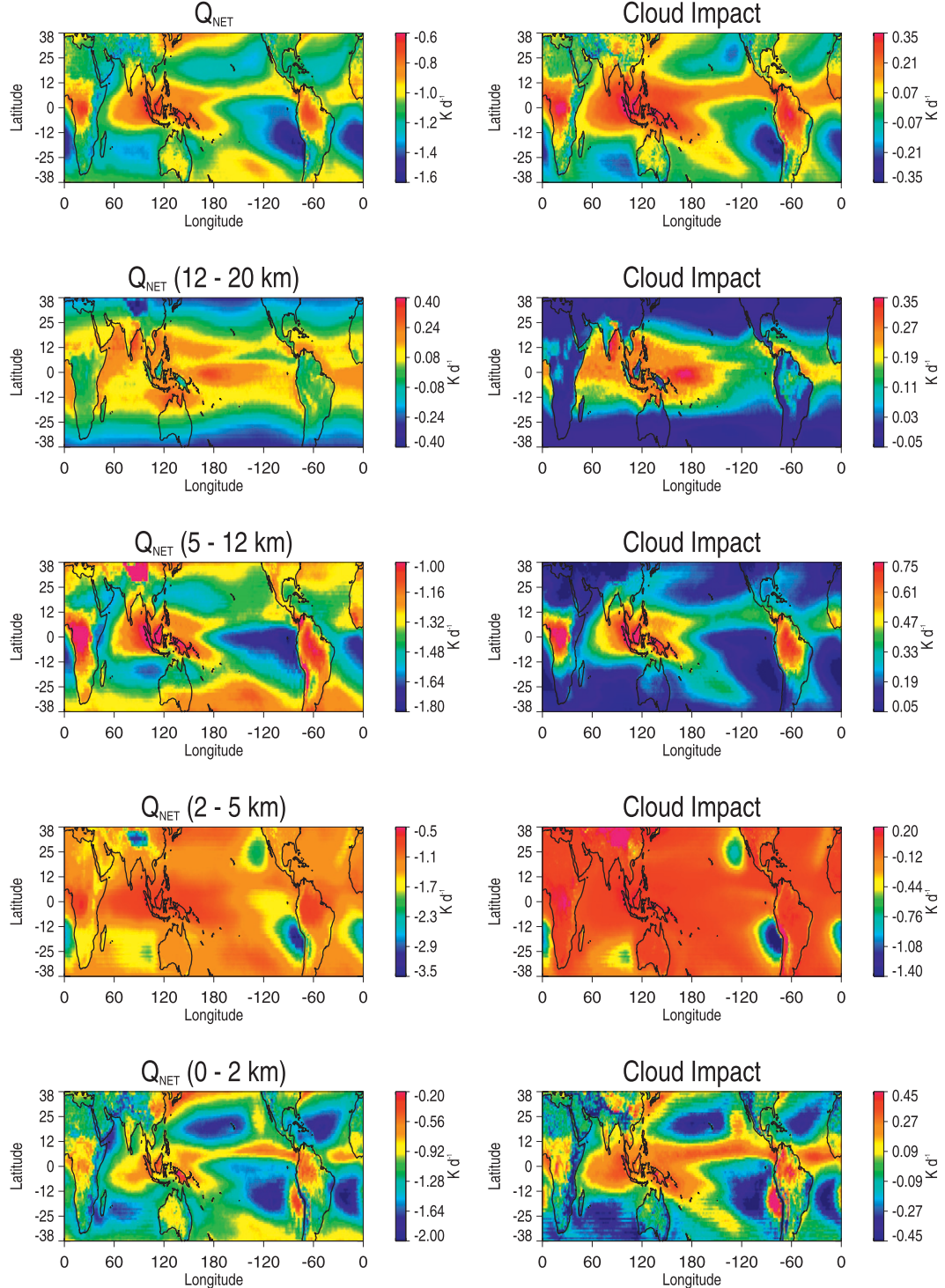


FIG. 9. As in Fig. 7, but for net atmospheric heating.

b. Regional heating structures

The vertical structure of atmospheric radiative heating for the three ocean and two land areas identified in

Fig. 3 are compared in Fig. 10, highlighting their responses to differences in the distribution of clouds and water vapor in each region. Longwave radiative cooling profiles, for example, are strongest and deepest in the

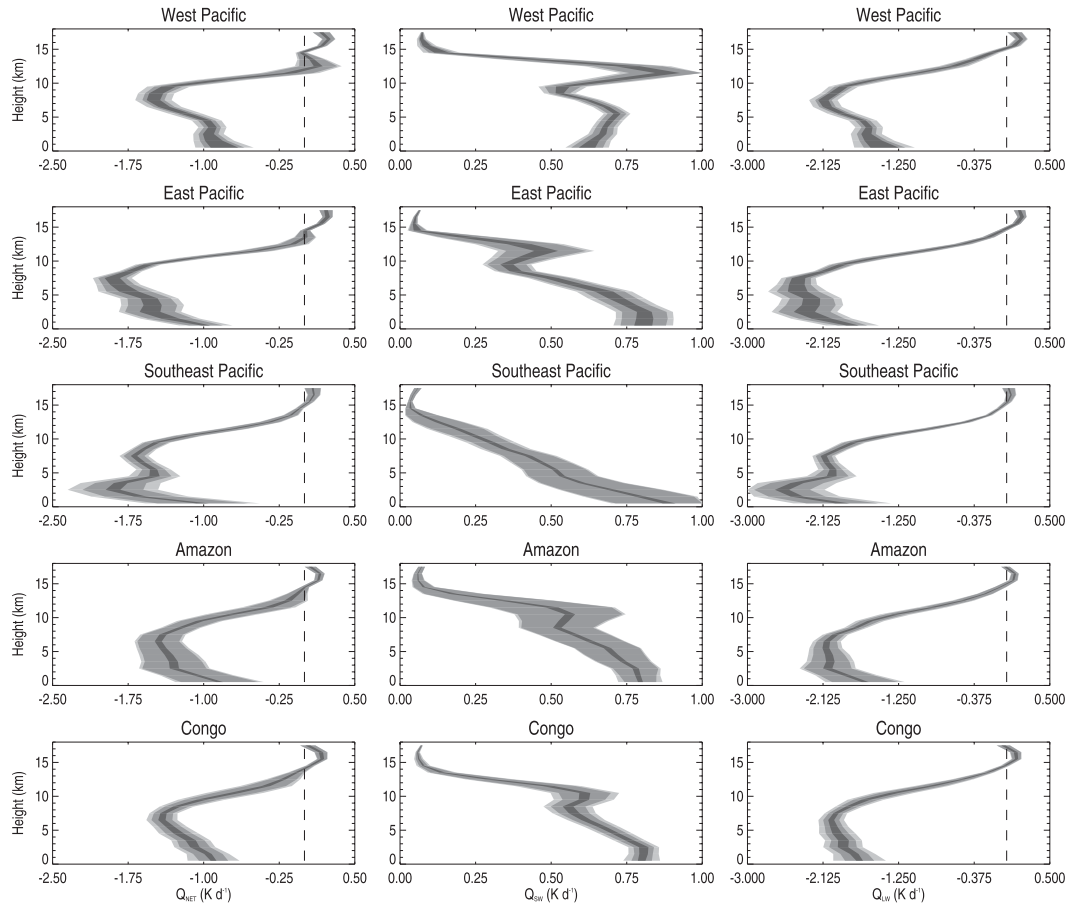


FIG. 10. Vertical profiles of (left) net heating and its breakdown into (middle) SW and (right) LW components for the five regions depicted in Fig. 3. Black bars represent the standard deviation of annually averaged heating rate profiles across each region, whereas the dark and light shades of gray represent monthly and five-day variability, respectively.

subsidence-dominated southeast Pacific (SEP; 10° – 30° S, 80° – 110° W), where cloud cover is dominated by shallow clouds that significantly enhance the radiation emitted to the surface relative to clear-sky conditions. Similarly, shortwave absorption is constrained to the lower atmosphere, falling off rapidly with height following the atmospheric water vapor profile. The net Q_R profile in the tropical east Pacific (TEP; 10° N– 10° S, 90° – 120° W) is also indicative of strong radiative cooling; however, unlike the SEP where low clouds are typically a factor of 3 more common than high clouds, high and low clouds occur with approximately equal likelihood in the TEP. As a result, the net cooling profile in the TEP shows evidence of enhanced SW heating at upper levels and reduced cooling at lower levels caused by a reduction in the emission of LW radiation to the surface by low clouds.

The distribution of high and low clouds reaches the opposite extreme in the convectively active TWP (10° N– 10° S, 140° – 170° E), where high-cloud fractions are

typically 55%–60%. This results in a significant deepening of the SW heating profile and reduced LW cooling at all heights, consistent with the much lower values of N and R_c observed in this region. The resulting net Q_R profile in the TWP is shallower than either the TEP or SEP regions and exhibits a sharper and weaker peak in net radiative cooling between 7 and 9 km.

The shallowest cooling profiles are found in the two continental regions, the Amazon (AMZ; 0° – 20° S, 50° – 80° W) and central Africa (AFR; 10° N– 10° S, 10° – 40° E). This reflects a combination of reduced water vapor amounts over land and the high incidence of cirrus clouds associated with deep convection that introduce significant upper-level LW heating (Fig. 8). This is particularly evident in the African region that is centered on the Congo, where the atmosphere is typically very dry; precipitation is dominated by electrically active deep convection (Petersen and Rutledge 2001); and net radiative cooling seldom exceeds -1 K day^{-1} , peaking at

less than -1.5 K day^{-1} at 7 km. Here, Q_{NET} profiles over the two continental regions strongly resemble that observed in the TWP, although SW heating at upper levels is more pronounced in the TWP, where convection occurs 20%–30% more frequently.

The regions depicted in Fig. 3 also exhibit distinct time scales of variability reflecting the different modes of forcing that dominate variations in their local meteorology. Interannual variability in the vertical structure of radiative heating in each region is indicated by the thickness of the central black lines in Fig. 10. Year-to-year variability in atmospheric radiative heating is generally small in the Amazon and southeast Pacific. Variations are larger in the west Pacific and Congo, where the frequencies of clouds and precipitation have been shown to vary on interannual time scales in response to ENSO (L'Ecuyer and Stephens 2007). The impacts of ENSO are greatest in the central and east Pacific, evidenced by the widest range of interannual variability in the atmospheric radiative heating profile in the TEP region. In part, this result reflects the fact that high-cloud fraction increased by more than 40% during the 1998 El Niño, whereas the frequency of low clouds was reduced by 15%. This produced a Q_R profile in the TEP from January–May 1998 that more closely resembled the TWP and is largely responsible for the increased interannual variability in the 10-yr HERB dataset.

Variations in the vertical structure of atmospheric radiative heating in monthly time scales is represented by the dark gray bars in Fig. 10. Seasonal cycles in solar insolation and the associated responses of high and low cloudiness (e.g., Fig. 6) dominate $Q_R(z)$ variability in the southeast Pacific and Amazon regions causing significant fluctuations in both SW and LW radiative heating profiles. As a result, the net heating profile in the lower troposphere can vary by more than 25% over the course of a year. Solar insolation is much less variable in the three remaining regions since they straddle the equator. This reduces seasonal changes in clouds and precipitation in both the Congo and the TWP; however, high-cloud anomalies associated with the southern branch of the double ITCZ (Lietzke et al. 2001) introduce some monthly variability in the TEP.

The light gray bars in Fig. 10 represent the standard deviation of five-day-averaged heating profiles, the shortest time scale that can be reasonably represented by the HERB dataset given the sampling characteristics of TRMM. Variability in these shorter time scales is generally more pronounced in LW heating rate profiles, suggesting a greater sensitivity to short-term changes in cloud cover. Shorter-term variations in atmospheric radiative heating rate profiles are largest (relative to other time scales) in the TWP and Congo, suggesting that some

level of convective organization exists on multiday time scales. These time scales of variability are loosely consistent with the propagation of the Madden–Julian oscillation (MJO) across the 30° TWP region and African easterly waves (AEWs) in the Congo (Wheeler and Kiladis 1999; Nguyen and Duvel 2008). The lack of a significant increase in heating rate variability in the Amazon, on the other hand, suggests that, although cloud cover may exhibit diurnal and day-to-day variations, these variations tend to be more randomly distributed over any given five-day period.

Variability in the vertical structure of atmospheric radiative heating in the Amazon is explored in more detail in Fig. 11. Immediately evident is the strong annual cycle, especially in shortwave and net heating that, to first order, correlates with solar insolation shown in Fig. 12. Annual variability dominates either longer (i.e., interannual) or shorter time-scale variations and clouds, precipitation, and vertical motion all exhibit strong annual cycles that tend to repeat with only minor differences from year to year (Fig. 12). For example, Q_{LW} exhibits a well-defined seasonal cycle, with peak cooling coinciding with the minimum in high-cloud fraction (and associated greenhouse effect) and peak in low-cloud fraction (and associated emission to the surface). SW heating exhibits a similar cycle, although the timing of peak solar heating shifts later in the year with increasing altitude. Near the surface, SW heating tends to precede the maximum in solar insolation by 1–2 months because of a trade-off between decreasing low-level cloudiness, which reaches a peak in winter months, and increasing solar insolation. Low clouds decrease to a minimum near the solar maximum offsetting the increased SW absorption by lower-level water vapor in midsummer. Upper-level clouds, on the other hand, reach a minimum in midwinter (July) and increase with solar insolation, reaching a peak in February, corresponding to peaks in convective precipitation and large-scale ascent in the middle of the Amazon wet season. Thus, the transition from low to high clouds coupled with a 30–45-day lag in high-cloud fraction relative to the solar cycle produces a Q_{sw} profile time series that slopes toward later peaks, with increasing altitude between the surface and 9 km in Fig. 11.

6. Conclusions

The 2008 version of the HERB algorithm provides estimates of vertical profiles of atmospheric radiative heating rates at 0.25° spatial and 1-km vertical resolution that are consistent with the observed distribution of clouds and precipitation from the TRMM satellite. Relative to the earlier versions of the algorithm, HERB

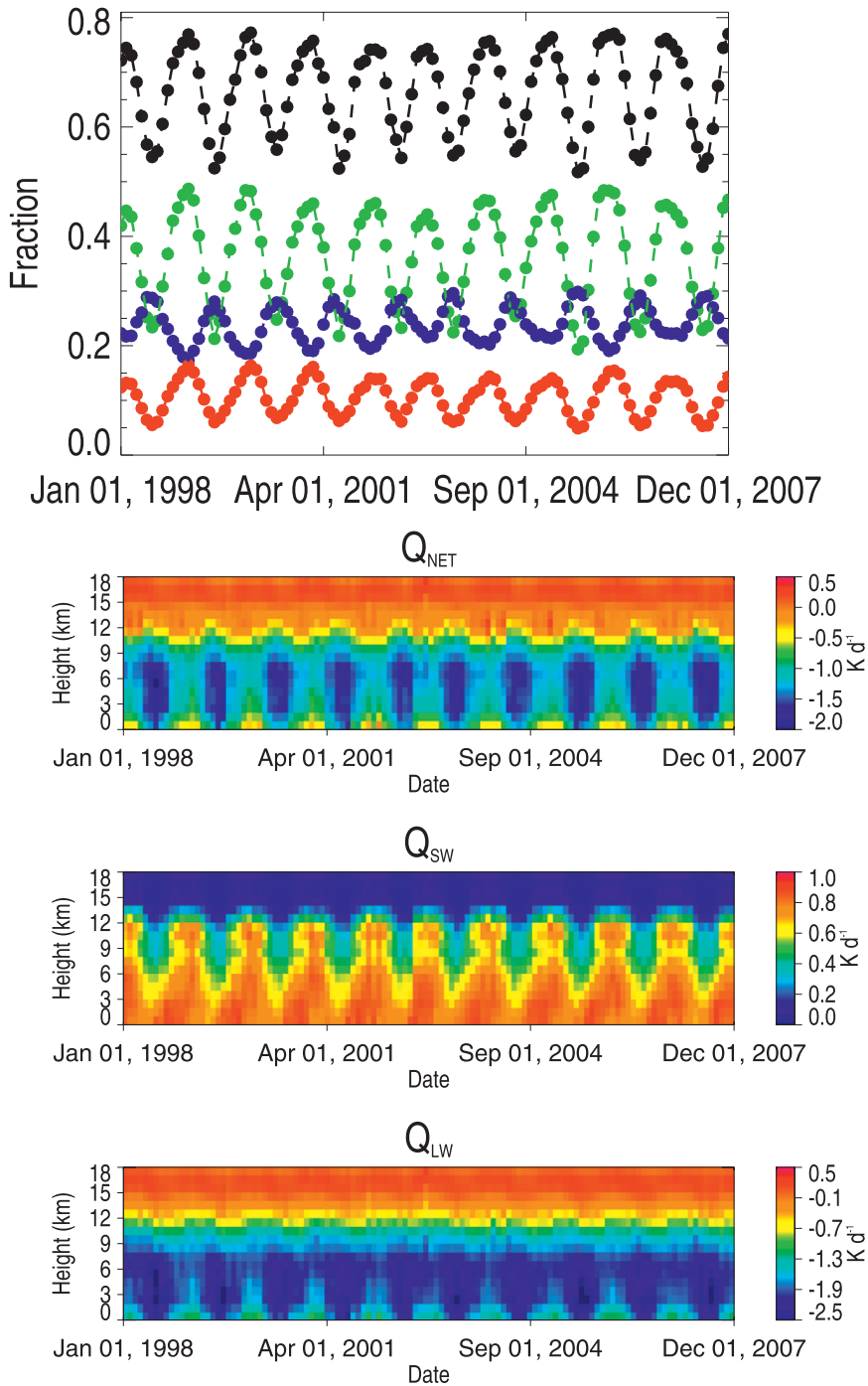


FIG. 11. (top) Time series of monthly-mean cloud fraction (black) and its decomposition into high cloud (green), low cloud (blue), and raining (red) pixels. (bottom) Time–height cross section of monthly-mean net (Q_{NET}), SW (Q_{SW}), and LW (Q_{LW}) heating in the Amazon region for the 10-yr period of January 1998–December 2007.

2008 applies over both land and ocean surfaces, provides an improved representation of clouds, and includes limited information concerning daily variations in aerosol concentrations based on output from the SPRINTARS

transport model. With these changes, biases in monthly-mean TOA fluxes at 5° resolution relative to CERES observations are less than 3% in the SW and 7 W m⁻² in the LW. Large-scale estimates of radiative fluxes at the

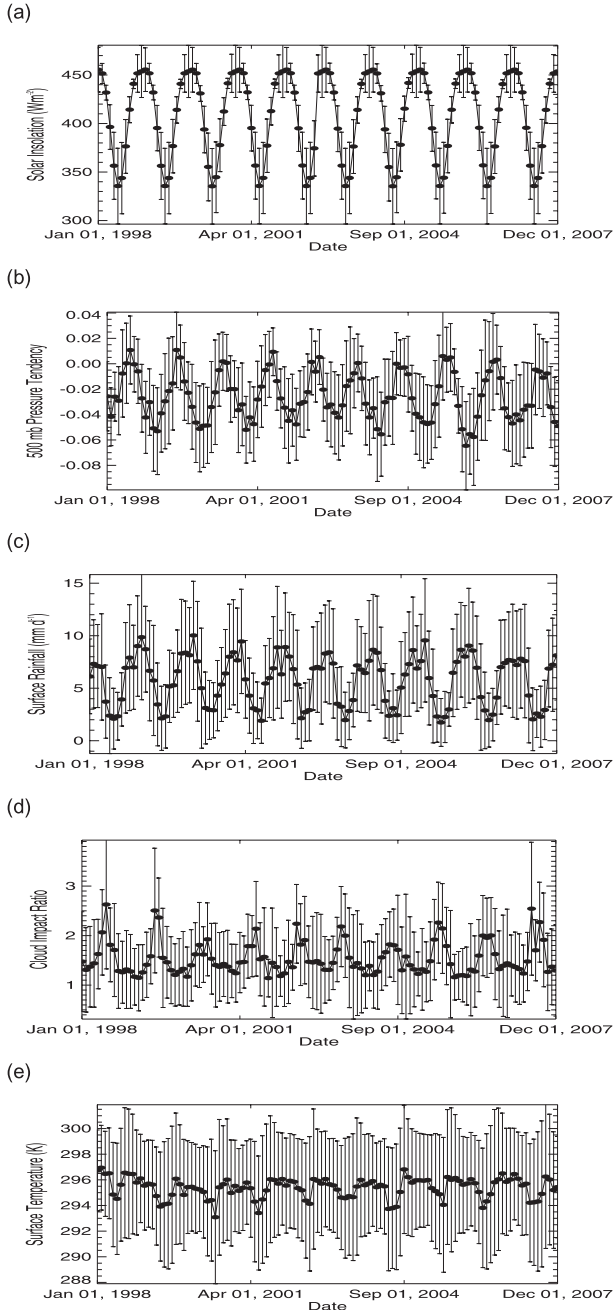


FIG. 12. (a) Solar insolation, (b) 500-mb vertical velocity in Pa s^{-1} , (c) surface rainfall, (d) cloud impact ratio, and (e) surface temperature in the Amazon region for the January 1998–December 2007 period. Uncertainty bars represent the spatial standard deviation of each variable across the domain.

surface and within the atmosphere exhibit a similar level of agreement with the estimates from the CERES CRS product. Given these favorable comparisons with CERES, the HERB product can be thought of as extending the eight-month CERES dataset over the full lifetime

of TRMM through a physically based flux retrieval scheme.

The results presented here provide a baseline climatology of $Q_R(z)$ in the tropical and subtropical atmospheres in the TRMM era. Examples of $Q_R(z)$ in five distinct regions illustrate the ability of the HERB dataset to capture the response of atmospheric radiative heating to regional differences in cloud morphology. A clear relationship emerges between the vertical structure of atmospheric radiative heating and large-scale vertical motion through its impact on the regional distribution of clouds and water vapor. Areas of persistent subsidence are characterized by deep profiles of strong net radiative cooling, often accompanied by extremely strong low-level cooling resulting from enhanced emission from liquid clouds. High clouds in convectively active regions lead to both the suppression of LW cooling aloft and a significant increase in the vertical extent of SW heating, resulting in a shallower net radiative cooling profile and peak cooling that is more than -0.5 K day^{-1} weaker than that in subsidence regions. Regional heating estimates also exhibit distinct responses to external forcings on different time scales, providing insights into the dominant modes of variability in any given region. Interannual variability resulting from ENSO, for example, is clearly evident in the tropical east Pacific, whereas the annual cycle of convection dominates variability in atmospheric heating in the Amazon. There is also evidence for multiday organization of clouds in the west Pacific and Congo, although specific mechanisms for this organization cannot be ascribed without further analysis.

The results suggest that, despite potential uncertainties in prescribed cloud boundaries, aerosol single-scattering properties and water vapor (over land), the distinct retrievals of high clouds, low clouds, and precipitation from visible, infrared, and microwave radiance observations provide sufficient constraints to resolve the vertical structure of atmospheric heating over a reduced number of coarse height bins, especially when longer time and larger spatial scales are analyzed. Estimates of column-integrated atmospheric radiative heating in distinct cloud regimes offer a means for constraining Q_R in simple models, whereas the full vertical profile and its spatial variability on different time scales can be used to evaluate more sophisticated models and to determine whether they exhibit appropriate variability in response to climate forcings on various scales (e.g., Soden 2000). Finally, when combined with corresponding TRMM-based estimates of latent heating, HERB products offer a unique opportunity to develop the first satellite-based estimates of the vertical structure of atmospheric diabatic heating.

Acknowledgments. This research was supported by NASA Energy and Water Cycle Sponsored Research (NEWS) Grant NAG06GC46G. All surface flux data were obtained through the CERES/ARM Validation Experiment (CAVE). ARM data are made available through the U.S. Department of Energy as part of the Atmospheric Radiation Measurement Program. GMD and SURFRAD data are made available through the NOAA/Earth System Research Laboratory/Global Monitoring Division–Radiation (G-RAD). CERES CRS data were obtained from the NASA Langley Research Center EOSDIS Distributed Active Archive Center.

REFERENCES

- Anderson, S. P., K. Huang, N. J. Brink, M. F. Baumgartner, and R. A. Weller, 2000: Pan American Climate Study (PACS) data report. Woods Hole Oceanographic Institution Tech. Rep. WHOI-2000-03, 151 pp.
- Augustine, J. A., J. J. DeLuisi, and C. N. Long, 2000: SURFRAD—A national surface radiation budget network for atmospheric research. *Bull. Amer. Meteor. Soc.*, **81**, 2341–2357.
- Bishop, J. K. B., W. B. Rossow, and G. Ellsworth, 1997: Surface solar irradiance from the International Satellite Cloud Climatology Project 1983–1991. *J. Geophys. Res.*, **102**, 6883–6910.
- Bony, S., J.-L. Dufresne, H. Le Treut, J.-J. Morcrette, and C. Senior, 2004: On dynamic and thermodynamic components of cloud changes. *Climate Dyn.*, **22**, 71–86.
- , and Coauthors, 2006: How well do we understand and evaluate climate change feedback processes? *J. Climate*, **19**, 3445–3482.
- Chen, T., W. B. Rossow, and Y. Zhang, 2000: Radiative effects of cloud-type variations. *J. Climate*, **13**, 264–285.
- Cooper, S. J., T. S. L'Ecuyer, and G. L. Stephens, 2003: The impact of explicit cloud boundary information on ice cloud microphysical property retrievals from infrared radiances. *J. Geophys. Res.*, **108**, 4107, doi:10.1029/2002JD002611.
- Feldman, D. R., T. S. L'Ecuyer, K. N. Liou, and Y. L. Yung, 2008: Remote sensing of tropical tropopause layer radiation balance using A-train measurements. *J. Geophys. Res.*, **113**, D21113, doi:10.1029/2008JD010158.
- Fu, Q., and K.-N. Liou, 1992: On the correlated k -distribution method for radiative transfer in nonhomogeneous atmospheres. *J. Atmos. Sci.*, **49**, 2139–2156.
- Grecu, M., and W. S. Olson, 2006: Bayesian estimation of precipitation from satellite passive microwave observations using combined radar–radiometer retrievals. *J. Appl. Meteor. Climatol.*, **45**, 416–433.
- Greenwald, T. J., G. L. Stephens, T. H. Vonder Haar, and D. L. Jackson, 1993: A physical retrieval of cloud liquid water over the global oceans using Special Sensor Microwave/Imager (SSM/I) observations. *J. Geophys. Res.*, **98**, 18 471–18 488.
- , C. L. Combs, A. S. Jones, D. L. Randel, and T. H. Vonder Haar, 1997: Further developments in estimating cloud liquid water over land using microwave and infrared satellite measurements. *J. Appl. Meteor.*, **36**, 389–405.
- Hartmann, D. L., H. H. Hendon, and R. A. Houze Jr., 1984: Some implications of the mesoscale circulations in tropical cloud clusters for large-scale dynamics and climate. *J. Atmos. Sci.*, **41**, 113–121.
- Houze, R. A., Jr., 1982: Cloud clusters and large-scale vertical motions in the tropics. *J. Meteor. Soc. Japan*, **60**, 396–409.
- , 1989: Observed structure of mesoscale convective systems and implications for large-scale heating. *Quart. J. Roy. Meteor. Soc.*, **115**, 425–461.
- Johnson, R. H., and P. E. Ciesielski, 2002: Characteristics of the 1998 summer monsoon onset over the northern South China Sea. *J. Meteor. Soc. Japan*, **80**, 561–578.
- Kalnay, E., and Coauthors, 1996: The NCEP/NCAR 40-Year Reanalysis Project. *Bull. Amer. Meteor. Soc.*, **77**, 437–471.
- Kummerow, C. D., and Coauthors, 2000: The status of the Tropical Rainfall Measuring Mission (TRMM) after two years in orbit. *J. Appl. Meteor.*, **39**, 1965–1982.
- Lau, K.-M., and L. Peng, 1987: Origin of low-frequency (intra-seasonal) oscillations in the tropical atmosphere. Part I: Basic theory. *J. Atmos. Sci.*, **44**, 950–972.
- L'Ecuyer, T. S., and G. L. Stephens, 2003: The tropical oceanic energy budget from the TRMM perspective. Part I: Algorithm and uncertainties. *J. Climate*, **16**, 1967–1985.
- , and —, 2007: The tropical atmospheric energy budget from the TRMM perspective. Part II: Evaluating GCM representations of the sensitivity of regional energy and water cycles to the 1998–99 ENSO cycle. *J. Climate*, **20**, 4548–4571.
- , N. B. Wood, T. Haladay, G. L. Stephens, and P. W. Stackhouse Jr., 2008: Impact of clouds on atmospheric heating based on the R04 CloudSat fluxes and heating rates data set. *J. Geophys. Res.*, **113**, D00A15, doi:10.1029/2008JD009951.
- Lee, M.-I., I.-S. Kang, J.-K. Kim, and B. E. Mapes, 2001: Influence of cloud-radiation interaction on simulating tropical intra-seasonal oscillation with an atmospheric general circulation model. *J. Geophys. Res.*, **106**, 14 219–14 233.
- Lietzke, C. E., C. Deser, and T. H. Vonder Haar, 2001: Evolutionary structure of the eastern double ITCZ based on satellite moisture profile retrievals. *J. Climate*, **14**, 743–751.
- Mapes, B. E., and R. A. Houze Jr., 1995: Diabatic divergence profiles in western Pacific mesoscale systems. *J. Atmos. Sci.*, **52**, 1807–1828.
- McClatchey, F. A., R. W. Fenn, J. E. Selby, F. E. Volz, and J. S. Goring, 1972: Optical properties of the atmosphere. 3rd ed. Air Force Cambridge Research Laboratory Tech. Rep. AFCLR-72-0497, 102 pp.
- McFarlane, S. A., J. H. Mather, and T. P. Ackerman, 2007: Analysis of tropical radiative heating profiles: A comparison of models and observations. *J. Geophys. Res.*, **112**, D14218, doi:10.1029/2006JD008290.
- Miles, N. L., J. Verlinde, and E. E. Clothiaux, 2000: Cloud droplet size distributions in low-level stratiform clouds. *J. Atmos. Sci.*, **57**, 295–311.
- Nguyen, H., and J. P. Duvel, 2008: Synoptic wave perturbations and convective systems over equatorial Africa. *J. Climate*, **21**, 6372–6388.
- Ohmura, A., and Coauthors, 1998: Baseline Surface Radiation Network (BSRN/WCRP): New precision radiometry for climate research. *Bull. Amer. Meteor. Soc.*, **79**, 2115–2136.
- Petersen, W. A., and S. A. Rutledge, 2001: Regional variability in tropical convection: Observations from TRMM. *J. Climate*, **14**, 3566–3586.
- Platnick, S., M. D. King, S. A. Ackerman, W. P. Menzel, B. A. Baum, J. C. Riedi, and R. A. Frey, 2003: The MODIS cloud products: Algorithms and examples from Terra. *IEEE Trans. Geosci. Remote Sens.*, **41**, 459–473.
- Ritter, B., and J.-F. Geleyn, 1992: A comprehensive radiation scheme for numerical weather prediction models with

- potential applications in climate simulations. *Mon. Wea. Rev.*, **120**, 303–325.
- Rossow, W. B., and A. A. Lacis, 1990: Global, seasonal cloud variations from satellite radiance measurements. Part II: Cloud properties and radiative effects. *J. Climate*, **3**, 1204–1253.
- , and Y.-C. Zhang, 1995: Calculation of surface and top of atmosphere radiative fluxes from physical quantities based on ISCCP data sets. 2. Validation and first results. *J. Geophys. Res.*, **100**, 1167–1197.
- Rutan, D. A., F. G. Rose, N. Smith, and T. P. Charlock, 2001: Validation dataset for CERES Surface and Atmospheric Radiation Budget (SARB). *WCRP/GEWEX Newsletter*, No. 11, International GEWEX Project Office, Silver Spring, MD, 11–12.
- Schumacher, C., R. A. Houze Jr., and I. Kraucunas, 2004: The tropical dynamical response to latent heating estimates derived from the TRMM precipitation radar. *J. Atmos. Sci.*, **61**, 1341–1358.
- Sekiguchi, M., and T. Nakajima, 2008: A k -distribution-based radiation code and its computational optimization for an atmospheric general circulation model. *J. Quant. Spectrosc. Radiat. Transfer*, **109**, 2779–2793, doi:10.1016/j.jqsrt.2008.07.013.
- Sherwood, S. C., V. Ramanathan, T. P. Barnett, M. K. Tyree, and E. Roeckner, 1994: Response of an atmospheric general circulation model to radiative forcing of tropical clouds. *J. Geophys. Res.*, **99**, 20 829–20 845.
- Shige, S., Y. N. Takayabu, W.-K. Tao, and R. E. Johnson, 2004: Spectral retrieval of latent heating profiles from TRMM PR data. Part I: Development of a model-based algorithm. *J. Appl. Meteor.*, **43**, 1095–1113.
- , —, —, and C.-L. Shie, 2007: Spectral retrieval of latent heating profiles from TRMM PR data. Part II: Algorithm improvement and heating estimates over tropical ocean regions. *J. Appl. Meteor. Climatol.*, **46**, 1098–1124.
- Slingo, A., and J. M. Slingo, 1988: The response of a general circulation model to cloud longwave radiative forcing. I: Introduction and initial experiments. *Quart. J. Roy. Meteor. Soc.*, **114**, 1027–1062.
- Slingo, J. M., and A. Slingo, 1991: The response of a general circulation model to cloud longwave radiative forcing. II: Further studies. *Quart. J. Roy. Meteor. Soc.*, **117**, 333–364.
- Smith, E. A., X. Xiang, A. Mugnai, and G. L. Tripoli, 1994: Design of an inversion-based precipitation profile retrieval algorithm using an explicitly cloud model for initial guess microphysics. *Meteor. Atmos. Phys.*, **54**, 53–78.
- Soden, B., 2000: The sensitivity of the tropical hydrological cycle to ENSO. *J. Climate*, **13**, 538–549.
- Stephens, G. L., 2005: Cloud feedbacks in the climate system: A critical review. *J. Climate*, **18**, 237–273.
- , P. M. Gabriel, and P. T. Partain, 2001: Parameterization of atmospheric radiative transfer. Part I: Validity of simple models. *J. Atmos. Sci.*, **58**, 3391–3409.
- Takemura, T., H. Okamoto, Y. Maruyama, A. Numaguti, A. Higurashi, and T. Nakajima, 2000: Global three-dimensional simulation of aerosol optical thickness distribution of various origins. *J. Geophys. Res.*, **105**, 17 853–17 873.
- , T. Nakajima, O. Dubovik, B. N. Holben, and S. Kinne, 2002: Single-scattering albedo and radiative forcing of various aerosol species with a global three-dimensional model. *J. Climate*, **15**, 333–352.
- , T. Nozawa, S. Emori, T. Y. Nakajima, and T. Nakajima, 2005: Simulation of climate response to aerosol direct and indirect effects with aerosol transport-radiation model. *J. Geophys. Res.*, **110**, D02202, doi:10.1029/2004JD005029.
- Tao, W.-K., J. Simpson, S. Lang, M. McCumber, R. Adler, and R. Penc, 1990: An algorithm to estimate the heating budget from vertical hydrometeor profiles. *J. Appl. Meteor.*, **29**, 1232–1244.
- , S. Lang, J. Simpson, and R. Adler, 1993: Retrieval algorithms for estimating the vertical profile of latent heat release. *J. Meteor. Soc. Japan*, **71**, 685–700.
- Tian, B., and V. Ramanathan, 2002: Role of tropical clouds in surface and atmospheric energy budget. *J. Climate*, **15**, 296–305.
- , and —, 2003: A simple moist tropical atmosphere model: The role of cloud radiative forcing. *J. Climate*, **16**, 2086–2092.
- Weaver, C. P., 1999: Interactions among cyclone dynamics, vertical thermodynamic structure, and cloud radiative forcing in the North Atlantic summertime storm track. *J. Climate*, **12**, 2625–2642.
- Wentz, F., 1997: A well-calibrated ocean algorithm for special sensor microwave/imager. *J. Geophys. Res.*, **102**, 8703–8718.
- , C. Gentemann, D. Smith, and D. Chelton, 2000: Satellite measurements of sea surface temperature through clouds. *Science*, **288**, 847–850.
- Wheeler, M., and G. N. Kiladis, 1999: Convectively coupled equatorial waves: Analysis of clouds and temperature in the wavenumber-frequency domain. *J. Atmos. Sci.*, **56**, 374–399.
- Wielicki, B. A., B. R. Barkstrom, E. F. Harrison, R. B. Lee III, G. L. Smith, and J. E. Cooper, 1996: Clouds and the Earth's Radiant Energy System (CERES): An earth observing system experiment. *Bull. Amer. Meteor. Soc.*, **77**, 853–868.
- Yuan, J., D. L. Hartmann, and R. Wood, 2008: Dynamic effects on the tropical cloud radiative forcing and radiation budget. *J. Climate*, **21**, 2337–2351.
- Zhang, M. H., J. L. Lin, R. T. Cederwall, J. J. Yio, and S. C. Xie, 2001: Objective analysis of ARM IOP data: Method and sensitivity. *Mon. Wea. Rev.*, **129**, 295–311.
- Zhang, Y.-C., W. B. Rossow, and A. A. Lacis, 1995: Calculation of surface and top of the atmosphere radiative fluxes from physical quantities based on ISCCP data sets. 1. Method and sensitivity to input data uncertainties. *J. Geophys. Res.*, **100**, 1149–1165.